
MPD²-Router: Mask-aware Multi-expert Prior-regularized Dual-head Deferral Router in Glaucoma Screening and Diagnosis

Wenxin Zhan
Baruch college
wenxin.zhan@baruchmail.cuny.edu

Abstract

Learning-to-defer (L2D) can make glaucoma screening safer by routing difficult/uncertain cases to humans, yet standard formulations overlook expert availability, heterogeneous readers behavior, workload imbalance, asymmetric diagnostic harm, case difficulty from morphology and deployment shift. We introduce MPD²-Router, a mask-aware multi-expert deferral framework that recasts ophthalmic triage as constrained human–AI routing: whether to defer and to which available expert. It couples a dual-head deferral/allocation policy with mask-aware Gumbel–sigmoid gating that strictly enforces per-sample availability, and fuses uncertainty, morphology, image-quality, and OOD signals. Training uses an asymmetric cost-sensitive objective with an augmented-Lagrangian deferral budget, a group-specific distribution prior, and a rank-majorization JS regularizer that jointly prevent expert collapse without forcing uniform allocation. Across three cross-national glaucoma cohorts (REFUGE, CHAKSU, ORIGA) with a frozen REFUGE-trained backbone, MPD²-Router substantially lowers clinical cost and improves MCC over AI-only at a moderate deferral rate. It is Pareto-optimal in F1–MCC–cost, robust under cross-domain shift, and yields balanced expert utilization.

1 Introduction

Artificial intelligence has achieved strong performance on ophthalmic image classification, yet the dominant formulation of the problem remains clinically incomplete and unsafe. Most existing systems are optimized as one-shot predictors: given an image, output a label. Real ophthalmic practice does not operate this way, it’s instead a *sequential decision process* under uncertainty, where clinicians must determine whether the available evidence is sufficient, whether additional imaging or testing is required, and whether a case should be escalated to another specialist. In other words, the clinically relevant question is not merely *what is the label*, but *what is the appropriate next action*. This mismatch between benchmark formulation and clinical workflow directly limits the safe integration of AI in ophthalmology.

Our study is motivated by two clinical realities often abstracted away in standard machine-learning benchmarks. First, human experts are fallible and heterogeneous rather than interchangeable oracles. Ophthalmologists, retina specialists, graders, and trainees differ in experience, subspecialty knowledge, decision thresholds, and tolerance for ambiguity; inter-grader variability can directly affect referral decisions.[Krause et al., 2018, Teoh et al., 2023]. Treating human review as a single noiseless reference, as much of the L2D literature implicitly does, discards precisely the structure that a safe routing system must model. Second, AI systems are not uniformly reliable. Confidence alone is a fragile triage signal: difficult morphology, low image quality, and out-of-distribution (OOD) inputs can significantly undermine calibration and accuracy. Together, these facts reframe glaucoma screening as a routing problem rather than a classification problem: *when should the system act autonomously, when should it defer, and to whom?*

Preprint.

L2D formalizes part of this problem by allowing a model to pass selected cases to a human decision-maker [Madras et al., 2018, Mozannar and Sontag, 2020], with recent extensions to calibrated, team-based, and multi-expert settings [Verma and Nalisnick, 2022, Mao et al., 2023]. However, existing formulations are largely built around generic and naive deployment assumptions, such as always-available human, an expert softmax with limited treatment of clinical cost and capacity. Glaucoma triage requires a richer formulation that accounts for per-sample expert feasibility, asymmetric diagnostic harm, morphology- and quality-dependent case difficulty, distribution shift, and the risk of concentrating deferred cases on scarce specialists. A useful glaucoma triage system should therefore be selective rather than indiscriminate, availability-aware rather than static, and Pareto-favorable: improving team-level utility without simply routing all hard cases to the same scarce expert.

Our contributions. We formulate glaucoma diagnosis as a constrained human–AI routing problem and make four contributions. First, we introduce a multi-signal deferral policy that conditions jointly on expert availability, AI uncertainty, optic-disc/cup morphology, image-quality risk, and OOD indicators. Second, we propose a dual-head router that separates *whether* to defer from *to whom* to defer, using mask-aware Gumbel–sigmoid support selection and masked expert allocation to enforce feasibility. Third, we regularize allocation with a group-specific empirical-Bayes-style competence prior and a rank-majorization JS penalty, mitigating expert collapse without forcing uniform routing. Fourth, we train under an asymmetric cost-sensitive objective with an augmented-Lagrangian deferral budget, yielding clinically aligned and workload-aware decisions. Together, MPD²-Router provides a clinically grounded framework for analyzing when autonomous AI is appropriate, when deferral is necessary, and how scarce expert attention should be allocated safely under shift.

2 Preliminaries

We study cost-sensitive ophthalmic triage with a frozen diagnostic predictor and a trainable multi-expert routing policy. Let $\mathcal{Y} = \{0, 1\}$, where $y = 1$ denotes glaucoma and $y = 0$ denotes non-glaucoma. Let $\mathcal{E} = \{1, \dots, M\}$ be the set of human experts. Action $a = 0$ retains the frozen AI prediction, while $a = j \in \mathcal{E}$ defers the case to expert j .

The routing training set is $\mathcal{D} = \{(x_i, y_i, \ell_i, \hat{y}_{i,1:M}, m_i^{\text{exp}})\}_{i=1}^N$, where $x_i \in \mathcal{X}$, $y_i \in \{0, 1\}$, $\ell_i = (\ell_i^{(0)}, \ell_i^{(1)}) \in \mathbb{R}^2$ are logits from a pretrained frozen AI classifier, and $p_i^{\text{ai}} = \text{Pr}_{\text{AI}}(y_i = 1 \mid x_i) = \text{softmax}(\ell_i)_1$. The expert label $\hat{y}_{i,j} \in \{0, 1, \text{NA}\}$ is observed only when expert j is feasible for sample i , encoded by $m_{i,j}^{\text{exp}} \in \{0, 1\}$, with $m_{i,j}^{\text{exp}} = 1 \iff j$ is feasible for sample i . The feasible expert set and feasible action set are $S_i = \{j \in \mathcal{E} : m_{i,j}^{\text{exp}} = 1\}$ and $\mathcal{A}_i = \{0\} \cup S_i$. Action 0 is always feasible; if $S_i = \emptyset$, we use the convention that $d_i = 0$ and the router deterministically selects action 0.

A stochastic router assigns $\pi_i = \pi_\theta(\cdot \mid x_i, m_i^{\text{exp}}) \in \Delta(\mathcal{A}_i)$, where the masked simplex is

$$\Delta(\mathcal{A}_i) = \{\pi \in \mathbb{R}_+^{M+1} : \sum_{a=0}^M \pi_a = 1, \pi_a = 0 \forall a \notin \mathcal{A}_i\}.$$

For $S_i \neq \emptyset$, any feasible policy admits the defer–allocate factorization $\pi_{i,0} = 1 - d_i$ and $\pi_{i,j} = d_i q_{i,j}$, where $d_i \in [0, 1]$ and

$$q_i \in \Delta(S_i) := \{q \in \mathbb{R}_+^M : \sum_{j \in S_i} q_j = 1, q_j = 0 \forall j \notin S_i\}.$$

Here d_i is the soft deferral mass and q_i is the conditional allocation distribution over feasible experts. Conversely, when $d_i > 0$, $q_{i,j} = \pi_{i,j} / \sum_{k=1}^M \pi_{i,k}$ and $d_i = 1 - \pi_{i,0} = \sum_{j=1}^M \pi_{i,j}$.

Soft routing quantities are optimization-facing. The empirical soft deferral rate is $\bar{d} = N^{-1} \sum_{i=1}^N d_i$, and the expert usage masses are $P_j^{\text{soft}} = N^{-1} \sum_{i=1}^N \pi_{i,j} = N^{-1} \sum_{i=1}^N d_i q_{i,j}$. At deployment, the stochastic policy is converted into the deterministic routing decision $\hat{a}_i = \arg \max_{a \in \mathcal{A}_i} \pi_{i,a}$, with ties broken in favor of the AI action. This induces the hard deferral indicator $d_i^{\text{hard}} = \mathbf{1}[\hat{a}_i \neq 0]$ and hard expert frequency $f_j^{\text{hard}} = N^{-1} \sum_{i=1}^N \mathbf{1}[\hat{a}_i = j]$. Thus d_i and \bar{d} are differentiable training quantities, whereas d_i^{hard} and f_j^{hard} describe realized deployment behavior.

We use an asymmetric clinical loss. For the frozen AI branch, $C_i^{\text{ai}} = c_{\text{fn}} y_i (1 - p_i^{\text{ai}}) + c_{\text{fp}} (1 - y_i) p_i^{\text{ai}}$, with $c_{\text{fn}} > c_{\text{fp}} > 0$. For feasible expert $j \in S_i$, $C_{i,j}^{\text{exp}} = c_{\text{fn}} \mathbf{1}[y_i = 1, \hat{y}_{i,j} = 0] + c_{\text{fp}} \mathbf{1}[y_i = 0, \hat{y}_{i,j} =$

1]. Let $\kappa_j \geq 0$ be the operational cost of expert j , with $\kappa_0 = 0$. For $\gamma \geq 0$, the expected per-sample routing loss is

$$L_i(\pi_i) = \pi_{i,0} C_i^{\text{ai}} + \sum_{j=1}^M \pi_{i,j} (C_{i,j}^{\text{exp}} + \gamma \kappa_j).$$

Under the defer-allocate factorization,

$$L_i(d_i, q_i) = (1 - d_i) C_i^{\text{ai}} + d_i \sum_{j=1}^M q_{i,j} (C_{i,j}^{\text{exp}} + \gamma \kappa_j) = C_i^{\text{ai}} + d_i \Delta_i(q_i),$$

where $\Delta_i(q_i) = \sum_{j=1}^M q_{i,j} (C_{i,j}^{\text{exp}} + \gamma \kappa_j) - C_i^{\text{ai}}$ is the marginal cost of replacing the AI decision by a deferred expert decision. The empirical clinical-operational risk is $\mathcal{L}_{\text{cost}}(\theta) = N^{-1} \sum_{i=1}^N L_i(d_i, q_i)$. The learning objective is to minimize this cost-sensitive routing risk under sample-dependent feasibility masks and a soft deferral budget $\bar{d} \leq \rho_{\text{def}}$. The next section specifies the mask-aware policy class and the regularizers used to stabilize multi-expert allocation under heterogeneous availability.

3 Method

We propose **MPD²-Router**, a mask-aware, prior-regularized dual-head router with policy

$$\pi_{\theta}(x_i, m_i^{\text{exp}}) = (1 - d_i, d_i q_i),$$

where $d_i \in (0, 1)$ denotes the probability of deferring case i to a human expert, and $q_i \in \Delta^{M-1}$ is a mask-aware conditional allocation distribution over feasible experts. Figure 2 in Appendix B provides the complete workflow schematic of MPD²-Router.

3.1 Router representation

The router state combines three sources of evidence: frozen AI logits, risk signals, and morphology-derived structural features. Let

$$P_i = \text{softmax}(\ell_i), \quad p_i^{\text{ai}} = P_{i,1}, \quad u_i = 1 - \max_{c \in \{0,1\}} P_{i,c}.$$

The risk vector is

$$r_i^{\text{risk}} = [\text{ViM}_i, r_i^{\text{qual}}, u_i] \in \mathbb{R}^3,$$

where ViM_i is the standardized Virtual-logit Matching score [Wang et al., 2022], r_i^{qual} is an image-quality risk score, and u_i is maximum-probability uncertainty.

Let $\xi_i^{\text{str}} = \begin{bmatrix} \text{vCDR}_i \\ \text{aCDR}_i \end{bmatrix}$ denote optic-disc/cup morphology. A scalar structural risk estimate is

$$p_i^{\text{str}} = \sigma(w_{\text{str}}^{\top} \xi_i^{\text{str}} + b_{\text{str}}),$$

and the structural feature vector is

$$r_i^{\text{str}} = [2p_i^{\text{str}} - 1, |p_i^{\text{ai}} - p_i^{\text{str}}|] \in \mathbb{R}^2.$$

The first coordinate is a centered morphology margin; the second measures AI-structure disagreement.

The branch encoders are

$$h_i^{\text{risk}} = \phi_{\text{risk}}(r_i^{\text{risk}}), \quad h_i^{\text{str}} = \phi_{\text{str}}(r_i^{\text{str}}), \quad h_i^{\text{ai}} = \phi_{\text{ai}}(\ell_i),$$

and the fused router representation is $h_i = \phi_{\text{fuse}}(h_i^{\text{risk}} \parallel h_i^{\text{str}} \parallel h_i^{\text{ai}})$.

3.2 Mask-aware dual-head policy

The policy is factorized into two coupled decisions:

- (i) whether to defer, (ii) how to allocate deferred mass across feasible experts.

The defer head maps h_i to a soft deferral mass

$$d_i = \mathbf{1}[|S_i| > 0] \sigma(f_{\text{def}}(h_i)) \in [0, 1].$$

The factor $\mathbf{1}[|S_i| > 0]$ enforces autonomous prediction when no expert is feasible.

The expert head is first parameterized through a shared expert trunk $z_i = \varphi(h_i)$, it then produces two sets of logits:

$$\gamma_i = W_g z_i + c_g \in \mathbb{R}^M, \quad \beta_i = W_a z_i + c_a \in \mathbb{R}^M,$$

where γ_i controls stochastic support selection and β_i controls allocation within the selected support.

Stage I: masked stochastic support selection. Feasibility is imposed before randomization by the extended-real masking map

$$\bar{\gamma}_{i,j} = \gamma_{i,j} + \log m_{i,j}^{\text{exp}} = \begin{cases} \gamma_{i,j}, & j \in S_i, \\ -\infty, & j \notin S_i, \end{cases}$$

Equivalently, the masked Bernoulli odds are $\zeta_{i,j} = \exp(\bar{\gamma}_{i,j}) = m_{i,j}^{\text{exp}} \exp(\gamma_{i,j})$. Using the Gumbel-max representation, let

$$G_{i,j}^{(1)}, G_{i,j}^{(0)} \stackrel{\text{i.i.d.}}{\sim} \text{Gumbel}(0, 1), \quad \eta_{i,j} = G_{i,j}^{(1)} - G_{i,j}^{(0)} \sim \text{Logistic}(0, 1).$$

Equivalently, in distribution,

$$\eta_{i,j} \stackrel{d}{=} \log U_{i,j} - \log(1 - U_{i,j}), \quad U_{i,j} \sim \text{Unif}(0, 1).$$

The hard Bernoulli gate can be written as

$$s_{i,j}^{\text{hard}} = \mathbf{1}[\bar{\gamma}_{i,j} + \eta_{i,j} \geq 0]. \quad (1)$$

Replacing the discontinuous Bernoulli gate by a Binary Concrete (Gumbel–sigmoid) relaxation gives

$$\begin{aligned} \tilde{s}_{i,j} &= \sigma\left(\frac{\bar{\gamma}_{i,j} + \eta_{i,j}}{\tau_g}\right) \\ &= \left(1 + \exp\left[-\frac{\log \zeta_{i,j} + \log U_{i,j} - \log(1 - U_{i,j})}{\tau_g}\right]\right)^{-1} \\ &= \frac{\zeta_{i,j}^{1/\tau_g} U_{i,j}^{1/\tau_g}}{\zeta_{i,j}^{1/\tau_g} U_{i,j}^{1/\tau_g} + (1 - U_{i,j})^{1/\tau_g}}, \quad \tau_g > 0. \end{aligned} \quad (2)$$

Thus masking is exact at both the hard and relaxed levels:

$$m_{i,j}^{\text{exp}} = 0 \implies \zeta_{i,j} = 0 \implies s_{i,j}^{\text{hard}} = \tilde{s}_{i,j} = 0 \quad \forall \tau_g > 0.$$

We use the straight-through estimator

$$s_{i,j}^{\text{ST}} = s_{i,j}^{\text{hard}} - \text{sg}(\tilde{s}_{i,j}) + \tilde{s}_{i,j},$$

where $\text{sg}(\cdot)$ denotes stop-gradient. The forward pass uses the hard selector $s_{i,j}^{\text{hard}}$, while the backward pass follows the pathwise Binary Concrete gradient. For every feasible expert $j \in S_i$, conditioning on the sampled noise and writing

$$a_{i,j}^g = \frac{\bar{\gamma}_{i,j} + \eta_{i,j}}{\tau_g}, \quad \tilde{s}_{i,j} = \sigma(a_{i,j}^g),$$

the map $\bar{\gamma}_{i,j} \mapsto \tilde{s}_{i,j}$ is C^∞ , and

$$\frac{\partial \tilde{s}_{i,j}}{\partial \bar{\gamma}_{i,j}} = \frac{1}{\tau_g} \tilde{s}_{i,j} (1 - \tilde{s}_{i,j}).$$

Consequently,

$$\nabla_{\theta} s_{i,j}^{\text{ST}} = \nabla_{\theta} \tilde{s}_{i,j} = \frac{1}{\tau_g} \tilde{s}_{i,j} (1 - \tilde{s}_{i,j}) \nabla_{\theta} \gamma_{i,j}, \quad j \in S_i,$$

and the gradient is identically zero for infeasible experts.

Stage II: masked expert allocation. Conditional on the feasible set, allocation logits are temperature-scaled and masked before normalization:

$$\bar{\beta}_{i,j} = \frac{\beta_{i,j}}{\tau_a} + \log m_{i,j}^{\text{exp}} = \begin{cases} \beta_{i,j}/\tau_a, & j \in S_i, \\ -\infty, & j \notin S_i, \end{cases} \quad \tau_a > 0.$$

For $k_i > 0$, the masked softmax allocation is

$$a_{i,j} = \frac{m_{i,j}^{\text{exp}} \exp(\beta_{i,j}/\tau_a)}{\sum_{k=1}^M m_{i,k}^{\text{exp}} \exp(\beta_{i,k}/\tau_a)}, \quad a_i \in \Delta(S_i).$$

Thus allocation mass is normalized only over experts that are actually feasible for case i .

Full policy. Since independent Bernoulli support selection can produce an empty selected set, we repair the realized forward support by falling back to the full feasible mask:

$$s_i^\# = \begin{cases} s_i^{\text{hard}}, & \mathbf{1}^\top s_i^{\text{hard}} > 0, \\ m_i^{\text{exp}}, & \mathbf{1}^\top s_i^{\text{hard}} = 0. \end{cases}$$

For $k_i > 0$, the conditional expert policy is the renormalized restriction of the masked allocation a_i to the repaired support:

$$q_{i,j} = \frac{a_{i,j} s_{i,j}^\#}{\sum_{k=1}^M a_{i,k} s_{i,k}^\#}, \quad j = 1, \dots, M. \quad (3)$$

Combining the soft deferral mass with the conditional expert distribution gives the full action policy

$$\pi_i = (1 - d_i, d_i q_i) \in \Delta(\mathcal{A}_i), \quad q_i \in \Delta(S_i), \quad \sum_{j=0}^M \pi_{i,j} = 1. \quad (4)$$

3.3 Group-specific distribution prior

GSDP regularizes deferred expert allocation at the group level. Each sample is assigned a hybrid group

$$g(i) = (f(i), c(i)) \in \{1, \dots, G\},$$

where $f(i)$ is an availability-support family induced by m_i^{exp} , and $c(i)$ is a within-family representation cluster. Define

$$\mathcal{I}_g = \{i : g(i) = g\}, \quad D_g = \sum_{i \in \mathcal{I}_g} d_i, \quad D_+ = \sum_{i=1}^N d_i, \quad \tilde{q}_{g,j} = D_g^{-1} \sum_{i \in \mathcal{I}_g} d_i q_{i,j} \quad (D_g > 0).$$

Thus \tilde{q}_g is the deferred-load-weighted allocation barycenter for group g .

Hierarchical empirical-Bayes-style prior. We construct \tilde{p}_g through a hierarchical empirical-Bayes-style shrinkage estimator that pools expert-reliability statistics from the global cohort to support families and then to fine-grained groups. For $S \subseteq \mathcal{T}$, let

$$\mathcal{A}_S = \{j : \exists i \in S \text{ s.t. } m_{i,j}^{\text{exp}} = 1\}, \quad b_{S,j} = c_{\text{fn}} \widehat{\text{FNR}}_{S,j}^{\text{Lap}} + c_{\text{fp}} \widehat{\text{FPR}}_{S,j}^{\text{Lap}} + \kappa_j.$$

For hierarchy level $\ell \in \{\text{glob}, \text{fam}, \text{grp}\}$, with eligible support $\mathcal{V}_S^{(\ell)} \subseteq \mathcal{A}_S$, define

$$\nu_{S,j}^{(\ell)} = \frac{\mathbf{1}[j \in \mathcal{V}_S^{(\ell)}] v_j \exp(-\tau_{\text{bad}} b_{S,j})}{\sum_{k \in \mathcal{V}_S^{(\ell)}} v_k \exp(-\tau_{\text{bad}} b_{S,k})}, \quad \hat{\nu}_S^{(\ell)} = (1 - u_\ell) \nu_S^{(\ell)} + u_\ell \text{Unif}(\mathcal{V}_S^{(\ell)}).$$

Here $v_j > 0$ is an optional capacity multiplier, $\tau_{\text{bad}} > 0$ controls concentration toward low-badness experts, and $u_\ell \in [0, 1]$ gives a uniform floor.

Let $\mathcal{T}_f = \{i : F_i = f\}$, $\mathcal{T}_g = \{i : G_i = g\}$, $n_f = |\mathcal{T}_f|$, $n_g = |\mathcal{T}_g|$, and $f(g)$ be the parent family. With $\alpha_{\mathcal{A}}$ denoting restriction to \mathcal{A} and renormalization, define

$$p^{\text{glob}} = \hat{\nu}_{\mathcal{T}}^{(\text{glob})}, \quad p_f \propto_{\mathcal{A}_{\mathcal{T}_f}} a_f \hat{\nu}_{\mathcal{T}_f}^{(\text{fam})} + (1 - a_f) p^{\text{glob}}, \quad p_g^{(0)} \propto_{\mathcal{A}_{\mathcal{T}_g}} a_g \hat{\nu}_{\mathcal{T}_g}^{(\text{grp})} + a_g^{\text{fam}} p_{f(g)} + \rho_{\text{glob}} p^{\text{glob}}.$$

The shrinkage weights are

$$a_f = \frac{n_f}{n_f + n_{\text{fam}}^{(0)}}, \quad a_g = \frac{n_g}{n_g + n_{\text{grp}}^{(0)}}, \quad a_g^{\text{fam}} = [1 - a_g - \rho_{\text{glob}}]_+.$$

Here $n_{\text{fam}}^{(0)}$ and $n_{\text{grp}}^{(0)}$ are pseudo-counts, while ρ_{glob} preserves global bleed-through for small or noisy groups. Finally,

$$\tilde{p}_g = p_g^{(0)} \in \Delta(\mathcal{A}_{\mathcal{T}_g}), \quad \tilde{p}_{g,j} = 0 \quad \forall j \notin \mathcal{A}_{\mathcal{T}_g}.$$

GSDP regularizer. For $\mathcal{G}_+ = \{g : D_g > 0\}$ and $\omega_g = D_g/D_+$, define, when $D_+ > 0$,

$$\mathcal{L}_{\text{GSDP}}(\theta) = \sum_{g \in \mathcal{G}_+} \omega_g D_{\text{KL}}(\tilde{q}_g \| \tilde{p}_g) = \sum_{g \in \mathcal{G}_+} \frac{D_g}{D_+} \sum_{j \in \mathcal{A}_{\mathcal{T}_g}} \tilde{q}_{g,j} \log \frac{\tilde{q}_{g,j}}{\tilde{p}_{g,j}},$$

and set $\mathcal{L}_{\text{GSDP}} = 0$ if $D_+ = 0$. Thus GSDP acts only on deferred mass, weights groups by effective deferred load, and shrinks each group allocation toward a reliability-weighted hierarchical prior.

3.4 Rank-majorization Jensen–Shannon regularizer

GSDP controls group-level allocation, but does not directly prevent sample-level concentration. We therefore regularize the sorted rank profile of q_i , independent of expert identity. For $k_i = |S_i| > 0$, define

$$r_i = \text{sort}_{\downarrow}(q_i|_{S_i}) = (r_{i,1}, \dots, r_{i,k_i}), \quad r_{i,1} \geq \dots \geq r_{i,k_i} \geq 0, \quad \sum_{t=1}^{k_i} r_{i,t} = 1. \quad (5)$$

For $\varrho \in (0, 1)$, the truncated geometric reference is

$$g_{k_i, \varrho}(t) = \frac{(1 - \varrho)\varrho^{t-1}}{1 - \varrho^{k_i}}, \quad t = 1, \dots, k_i.$$

Let

$$R_i(t) = \sum_{s=1}^t r_{i,s}, \quad G_i(t) = \sum_{s=1}^t g_{k_i, \varrho}(s), \quad \chi_i = \mathbf{1} \left[\max_{1 \leq t \leq k_i} (R_i(t) - G_i(t)) > m_{\text{maj}} \right].$$

Thus the penalty activates only when q_i places excessive cumulative mass on the largest ranks. With

$$b_i^* = \frac{1}{2}(r_i + g_{k_i, \varrho}), \quad b_{i,t}^* = \frac{1}{2}(r_{i,t} + g_{k_i, \varrho}(t)),$$

the rank-profile Jensen–Shannon divergence is

$$\text{JS}(r_i \| g_{k_i, \varrho}) = \frac{1}{2} \sum_{t=1}^{k_i} \left[r_{i,t} \log \frac{r_{i,t}}{b_{i,t}^*} + g_{k_i, \varrho}(t) \log \frac{g_{k_i, \varrho}(t)}{b_{i,t}^*} \right].$$

The deferred-mass-weighted rank regularizer is, for $D_+ > 0$,

$$\mathcal{L}_{\text{rank}}(\theta) = \frac{1}{D_+} \sum_{i=1}^N d_i \chi_i \text{JS}(r_i \| g_{k_i, \varrho}),$$

and $\mathcal{L}_{\text{rank}} = 0$ if $D_+ = 0$. Hence the penalty acts on the conditional expert allocation only in proportion to the sample’s soft deferral mass.

3.5 Soft deferral control and full objective

Let $\bar{d} = N^{-1} \sum_{i=1}^N d_i$. For fixed q_i , increasing the soft deferral mass d_i is cost-improving exactly when the expert-side cost advantage over the AI action is negative. To prevent cost minimization from over-concentrating deferrals under sparse labels and heterogeneous masks, we optimize a GSDP/Rank-JS-regularized objective together with a one-sided augmented-Lagrangian deferral controller for the soft operational budget $\bar{d} \leq \rho_{\text{def}}$:

$$\begin{aligned} \min_{\theta} \mathcal{J}(\theta, \lambda_{\text{def}}) &= \frac{1}{N} \sum_{i=1}^N \left[C_i^{\text{ai}} + d_i \left(\sum_{j=1}^M q_{i,j} (C_{i,j}^{\text{exp}} + \gamma \kappa_j) - C_i^{\text{ai}} \right) \right] \\ &+ \lambda_{\text{GSDP}} \mathcal{L}_{\text{GSDP}}(\theta) + \lambda_{\text{rank}} \mathcal{L}_{\text{rank}}(\theta) + \lambda_{\text{def}} (\bar{d} - \rho_{\text{def}}) + \frac{\mu}{2} [\bar{d} - \rho_{\text{def}}]_+^2, \end{aligned} \quad (6)$$

where $\lambda_{\text{GSDP}}, \lambda_{\text{rank}} \geq 0$, $\lambda_{\text{def}} \geq 0$ is the augmented-Lagrangian multiplier, and $\mu > 0$ controls the quadratic penalty for budget violation. After each epoch, the deferral multiplier is updated by projected ascent,

$$\lambda_{\text{def}} \leftarrow [\lambda_{\text{def}} + \eta_{\lambda} (\bar{d} - \rho_{\text{def}})]_+.$$

4 Experiments

Datasets and benchmark construction. We evaluate on three glaucoma cohorts: REFUGE [Fang et al., 2022], CHAKSU [Kumar et al., 2023], and ORIGA [Zhang et al., 2010]. The base AI classifier is a SwinV2 model [Liu et al., 2022] trained only on the REFUGE training split and kept frozen during router training and evaluation, allowing us to study deferral under cross-cohort deployment shift. The cohorts provide heterogeneous supervision: CHAKSU includes native decisions from five ophthalmologists, REFUGE contains expert optic-disc and optic-cup annotations, and ORIGA has no native expert decisions. We treat the CHAKSU and REFUGE graders as disjoint experts, yielding a unified expert set of size $M = 12$. Each sample is assigned an availability mask m_i^{exp} , where $m_{i,j}^{\text{exp}} = 1$ iff expert j has a decision for sample i . Pseudo-labeling and dataset-specific supervision details are provided in Appendix E.

Table 1: Overall and dataset-wise test performance. All methods are evaluated on the same overall test set ($N = 899$); dataset sizes are REFUGE ($N = 400$), CHAKSU ($N = 336$), and ORIGA ($N = 163$). MPD²-Router achieves the strongest overall performance and remains robust across shifted cohorts.

(a) Overall test performance.

Method	Acc	Prec	F1	Sens	Spec	MCC	Defer	ClinicalCost	ExpertCost	TotalCost
AI-Only	0.755	0.370	0.530	0.932	0.725	0.482	0.000	0.372	0.000	0.372
Mao-TwoStage	0.925	0.726	0.760	0.797	0.948	0.717	0.403	0.127	0.084	0.211
Narasimhan-PH	0.937	0.764	0.794	0.827	0.956	0.758	0.388	0.108	0.079	0.187
Verma-OvA	0.949	0.813	0.831	0.850	0.966	0.801	0.747	0.088	0.200	0.288
Hemmer-MoE	0.949	0.804	0.833	0.865	0.963	0.804	0.626	0.087	0.185	0.271
Keswani-Joint Committee	0.932	0.786	0.764	0.744	0.965	0.725	0.468	0.121	0.143	0.264
MPD²-Router	0.960	0.849	0.868	0.887	0.973	0.844	0.437	0.068	0.113	0.181

(b) Dataset-wise test performance.

Method	Dataset	Acc	Prec	F1	Sens	Spec	MCC	Defer	ClinicalCost	ExpertCost	TotalCost
AI-Only	REFUGE	0.882	0.458	0.618	0.950	0.875	0.610	0.000	0.179	0.000	0.179
	CHAKSU	0.732	0.353	0.511	0.922	0.698	0.455	0.000	0.408	0.000	0.408
	ORIGA	0.491	0.328	0.484	0.929	0.339	0.263	0.000	0.773	0.000	0.773
Mao-TwoStage	REFUGE	0.938	0.642	0.731	0.850	0.947	0.705	0.220	0.101	0.053	0.154
	CHAKSU	0.940	0.816	0.800	0.784	0.968	0.765	0.470	0.106	0.081	0.186
	ORIGA	0.865	0.727	0.744	0.762	0.901	0.653	0.712	0.233	0.168	0.401
Narasimhan-PH	REFUGE	0.950	0.692	0.783	0.900	0.956	0.763	0.180	0.080	0.041	0.121
	CHAKSU	0.949	0.886	0.821	0.765	0.982	0.795	0.470	0.094	0.081	0.175
	ORIGA	0.877	0.729	0.778	0.833	0.893	0.697	0.730	0.206	0.168	0.374
Verma-OvA	REFUGE	0.960	0.773	0.810	0.850	0.972	0.788	0.598	0.068	0.175	0.243
	CHAKSU	0.940	0.782	0.811	0.843	0.958	0.777	0.866	0.101	0.206	0.307
	ORIGA	0.939	0.900	0.878	0.857	0.967	0.838	0.871	0.110	0.249	0.360
Hemmer-MoE	REFUGE	0.953	0.756	0.765	0.775	0.972	0.739	0.465	0.083	0.133	0.215
	CHAKSU	0.943	0.776	0.826	0.882	0.954	0.794	0.688	0.094	0.213	0.306
	ORIGA	0.951	0.886	0.907	0.929	0.959	0.874	0.896	0.083	0.254	0.337
Keswani-Joint Committee	REFUGE	0.945	0.765	0.703	0.650	0.978	0.675	0.110	0.100	0.032	0.132
	CHAKSU	0.938	0.742	0.814	0.902	0.944	0.782	0.866	0.101	0.268	0.370
	ORIGA	0.890	0.900	0.750	0.643	0.975	0.698	0.528	0.212	0.157	0.369
MPD²-Router	REFUGE	0.975	0.857	0.878	0.900	0.983	0.864	0.245	0.043	0.070	0.113
	CHAKSU	0.958	0.878	0.860	0.843	0.979	0.836	0.491	0.074	0.114	0.188
	ORIGA	0.926	0.812	0.867	0.929	0.926	0.820	0.798	0.120	0.215	0.335

4.1 Experiment Results

Overall comparison. Table 1a shows that MPD²-Router achieves the most favorable system-level trade-off among the compared selective-prediction and learning-to-defer methods. Relative to AI-only inference, it improves accuracy from 0.755 to 0.960, F1 from 0.530 to 0.868, and MCC from 0.482 to 0.844, while reducing clinical cost from 0.372 to 0.068. This improvement is clinically meaningful because the router reduces high-cost autonomous AI errors rather than merely increasing average predictive performance. Importantly, the gain is not driven by indiscriminate review: MPD²-Router defers 43.7% of cases, compared with 74.7% for Verma-OvA and 62.6% for Hemmer-MoE, and its spatial deferral pattern concentrates on regions where the frozen AI is unreliable rather than spreading uniformly across the test distribution (Appendix Fig. 7). In the F1–cost and MCC–cost planes, MPD²-Router is Pareto-favorable: no competing method simultaneously attains higher predictive utility and lower total cost (Appendix G.2).

Dataset-wise robustness. Table 1b further disaggregates performance across REFUGE, CHAKSU, and ORIGA. MPD²-Router attains the lowest total cost on REFUGE and ORIGA, and remains close to the best method on CHAKSU, while maintaining strong F1 and MCC across all three cohorts. The ORIGA results are particularly informative because the frozen AI degrades sharply under distribution shift, with accuracy falling to 0.491 and clinical cost rising to 0.773. MPD²-Router recovers ORIGA performance to 0.926 accuracy, 0.867 F1, and 0.820 MCC, while reducing clinical cost to 0.120 and achieving the lowest total cost. Competing methods can obtain high per-domain accuracy or F1, but often at the price of substantially higher deferral and expert cost; for example, Hemmer-MoE defers 89.6% of ORIGA cases. Thus, MPD²-Router provides a more deployable operating point: it

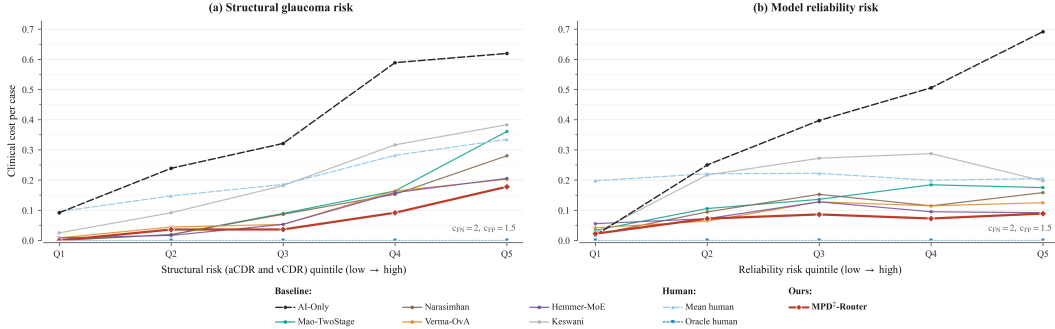


Figure 1: Risk-stratified clinical cost under structural glaucoma risk and model-reliability risk. Structural risk is defined by aCDR and vCDR quintiles, whereas reliability risk is defined by OOD and AI-uncertainty signals. MPD²-Router exhibits slower cost growth than most baselines and remains markedly below AI-Only in the highest-risk strata.

Table 2: Expert-collapse diagnostics over human-routed samples. Top-1 Share / Top-2 Share are the routed-case fractions assigned to the most-used and two most-used experts; lower Entropy-Collapse and Gini_{norm} and higher N_{eff} (number of effective experts) all indicate less concentrated routing.

Method	Routed n	Top-1 Share ↓	Top-2 Share ↓	Entropy-Collapse ↓	N_{eff} ↑	Gini _{norm} ↓
Mao-TwoStage	362	0.340	0.594	0.300	4.352	0.692
Narasimhan-PH	349	0.255	0.458	0.211	6.093	0.586
Verma-OvA	672	0.339	0.679	0.378	3.750	0.759
Hemmer-MoE	563	0.506	0.790	0.480	2.816	0.839
Keswani-Joint Committee	421	0.876	0.976	0.822	1.284	0.973
MPD²-Router	393	0.247	0.440	0.225	6.027	0.595

is not uniformly best on every isolated metric, but it yields consistently strong, cost-sensitive, and shift-robust routing decisions.

Risk-stratified robustness. Figure 1 stratifies samples along two clinically meaningful axes and compares MPD²-Router against baselines and the available human experts. Under model-reliability risk, defined by OOD and AI-uncertainty signals, the mean available-human cost remains relatively stable across quintiles, whereas AI-Only deteriorates sharply as reliability risk increases. Under structural glaucoma risk, clinical cost increases for nearly all methods, indicating that genuine clinical difficulty for both automated and human predictors. MPD²-Router is comparatively resilient on both axes: its cost grows more slowly than most baselines and remains substantially below AI-Only in the highest-risk quintiles.

Expert collapse diagnostic. Table 2 examines whether human-routed cases concentrate on a small subset of experts. MPD²-Router attains the lowest Top-1 share (24.7%) and Top-2 shares (44.0%), indicating that its gains do not stem from collapse onto a dominant reader. While MPD²-Router does not dominate Narasimhan-PH on every diversity metric, strict uniformity is neither clinically necessary nor desirable; the appropriate criterion is the avoidance of pathological concentration while preserving cost- and availability-aware allocation. By this measure, MPD²-Router’s diversity profile remains close to Narasimhan-PH and substantially improves over Hemmer-MoE and Keswani-Joint Committee, both of which exhibit severe routing concentration.

4.2 Ablation studies

We conducted three complementary ablation studies to isolate the contribution of the objective terms, the routing-regularization losses, and the augmented-Lagrangian (AL) deferral controller.

The objective ablation in Table 3a attains the most clinically meaningful operating point: it preserves strong predictive performance while keeping expert cost and deferral under control. Removing the tier-cost term yields marginally higher F1/MCC within one standard deviation, but this improvement is operationally expensive, increasing ExpertCost from 0.133 to 0.169 and raising soft deferral from 0.517 to 0.633. The clinical-only variant is more problematic: it nearly collapses into indiscriminate deferral (96.4%), substantially higher ExpertCost 0.259, and worse Acc/F1/MCC.

Table 3: Ablation studies on the test set. (a) Objective ablation; (b) routing-regularisation ablation; (c) augmented-Lagrangian deferral-control. Each entry reports mean \pm standard deviation over 10 random seeds. Lower Top1/Top2 Share, HHI, LoadCV, and DeadFrac, and higher EffExp/Entropy, indicate better expert utilisation. In (c), Gap is corresponding defer minus the requested target.

(a) Objective ablation.

Condition	$\mathcal{L}_{\text{clin}}$	ExpertCost	Defer _{soft}	Defer _{hard}	Sens.	Spec.	Acc	F1	MCC
Full objective	0.091 \pm 0.009	0.133 \pm 0.008	0.517 \pm 0.031	0.477 \pm 0.020	0.851 \pm 0.023	0.963 \pm 0.006	0.947 \pm 0.006	0.825 \pm 0.018	0.794 \pm 0.021
w/o Tier loss	0.089 \pm 0.009	0.169 \pm 0.014	0.633 \pm 0.052	0.516 \pm 0.024	0.862 \pm 0.022	0.962 \pm 0.004	0.947 \pm 0.005	0.829 \pm 0.016	0.799 \pm 0.019
Clinical only	0.108 \pm 0.012	0.259 \pm 0.019	0.959 \pm 0.053	0.964 \pm 0.109	0.867 \pm 0.018	0.946 \pm 0.011	0.934 \pm 0.008	0.797 \pm 0.019	0.762 \pm 0.022
w/o GSDP	0.093 \pm 0.013	0.139 \pm 0.009	0.536 \pm 0.038	0.485 \pm 0.016	0.848 \pm 0.017	0.962 \pm 0.008	0.945 \pm 0.008	0.822 \pm 0.024	0.790 \pm 0.028
w/o Rank-JS	0.094 \pm 0.009	0.134 \pm 0.011	0.520 \pm 0.040	0.478 \pm 0.019	0.853 \pm 0.021	0.961 \pm 0.006	0.945 \pm 0.005	0.820 \pm 0.016	0.789 \pm 0.019
w/o GSDP + Rank-JS	0.091 \pm 0.009	0.139 \pm 0.008	0.523 \pm 0.026	0.486 \pm 0.016	0.856 \pm 0.020	0.962 \pm 0.006	0.946 \pm 0.005	0.825 \pm 0.016	0.795 \pm 0.019

(b) Routing-regularisation ablation.

Condition	$\mathcal{L}_{\text{clin}}$	Defer _{soft}	Defer _{hard}	Top _{1share}	Top _{2share}	HHI _{norm}	LoadCV _{soft}	DeadFrac _{soft}	EffExp	Entropy
Full regularisation	0.091 \pm 0.009	0.517 \pm 0.031	0.477 \pm 0.020	0.371 \pm 0.062	0.591 \pm 0.083	0.086 \pm 0.016	0.971 \pm 0.091	0.208 \pm 0.067	7.603 \pm 0.521	0.815 \pm 0.028
w/o GSDP	0.093 \pm 0.013	0.536 \pm 0.038	0.485 \pm 0.016	0.455 \pm 0.067	0.680 \pm 0.085	0.123 \pm 0.024	1.159 \pm 0.111	0.233 \pm 0.050	6.754 \pm 0.497	0.768 \pm 0.030
w/o Rank-JS	0.094 \pm 0.009	0.520 \pm 0.040	0.478 \pm 0.019	0.398 \pm 0.057	0.619 \pm 0.082	0.094 \pm 0.018	1.011 \pm 0.094	0.250 \pm 0.065	7.371 \pm 0.500	0.803 \pm 0.028
w/o GSDP + Rank-JS	0.091 \pm 0.009	0.523 \pm 0.026	0.486 \pm 0.016	0.493 \pm 0.068	0.714 \pm 0.074	0.164 \pm 0.044	1.334 \pm 0.174	0.242 \pm 0.069	6.082 \pm 0.680	0.724 \pm 0.046

(c) Augmented-Lagrangian deferral-control.

Condition	Target	Defer _{soft}	Defer _{hard}	Gap _{soft}	Gap _{hard}	$\mathcal{L}_{\text{total}}$	$\mathcal{L}_{\text{clin}}$	Acc	F1
AL25	0.250	0.239 \pm 0.007	0.201 \pm 0.006	-0.011 \pm 0.007	-0.049 \pm 0.006	0.176 \pm 0.007	0.162 \pm 0.007	0.897 \pm 0.005	0.721 \pm 0.010
AL30	0.300	0.281 \pm 0.012	0.236 \pm 0.014	-0.019 \pm 0.012	-0.064 \pm 0.014	0.156 \pm 0.011	0.139 \pm 0.012	0.913 \pm 0.008	0.751 \pm 0.017
AL40	0.400	0.371 \pm 0.006	0.342 \pm 0.009	-0.029 \pm 0.006	-0.058 \pm 0.009	0.124 \pm 0.009	0.098 \pm 0.010	0.942 \pm 0.006	0.813 \pm 0.018
AL50	0.500	0.439 \pm 0.010	0.417 \pm 0.015	-0.061 \pm 0.010	-0.083 \pm 0.015	0.128 \pm 0.010	0.097 \pm 0.010	0.943 \pm 0.006	0.814 \pm 0.018
AL60	0.600	0.491 \pm 0.023	0.459 \pm 0.022	-0.109 \pm 0.023	-0.141 \pm 0.022	0.125 \pm 0.011	0.091 \pm 0.011	0.947 \pm 0.007	0.825 \pm 0.020
AL70	0.700	0.517 \pm 0.031	0.477 \pm 0.020	-0.183 \pm 0.031	-0.223 \pm 0.020	0.126 \pm 0.010	0.091 \pm 0.009	0.947 \pm 0.006	0.825 \pm 0.018
NoAL	-	0.535 \pm 0.034	0.503 \pm 0.008	-	-	0.127 \pm 0.009	0.092 \pm 0.009	0.946 \pm 0.006	0.824 \pm 0.016

In contrast, ablating GSDP, Rank-JS, or both yields only negligible changes in predictive performance, indicating that these routing regularizers do not achieve routing diversity by sacrificing diagnostic accuracy. Instead they act primarily on expert-utilisation structure and improve reliability of the learned policy. Table 3b supports this interpretation. Removing GSDP increases Top_{1share} from 0.371 to 0.455 and lowers the effective number of experts from 7.603 to 6.754, while removing Rank-JS produces a milder but similar concentration effect. Removing both regularizers is substantially worse: Top_{1share} rises to 0.493, Top_{2share} to 0.714, HHI_{norm} nearly doubles, and entropy drops from 0.815 to 0.724. Hence, GSDP and Rank-JS act complementarily: GSDP anchors group-level allocation to clinically informed priors, while Rank-JS discourages sample-level top-heavy routing, together preventing expert collapse without materially sacrificing clinical performance.

The augmented-Lagrangian in Table 3c demonstrates that deferral is controllable rather than an uncontrolled byproduct of the learned router. As the requested target increases from 0.25 to 0.70, the realized soft deferral rises monotonically from 0.239 to 0.517, with corresponding increases in hard deferral. The negative gaps indicate that the learned policy satisfies the request upper target and remains conservative relative to the targets, which is clinically preferable and pragmatic to systematic over-deferral. Importantly, performance is only meaningfully degraded under very restrictive budgets such as AL25/AL30, where the router is forced to retain too many difficult cases; once the budget enters a clinically useful range, the model recovers strong performance, with AL40–AL70 giving Acc 0.942–0.947 and F1 0.813–0.825, close to the unconstrained NoAL result. This supports the claim that the AL term provides practical deferral control with limited performance compromise in the relevant operating regime.

5 Conclusion

We presented MPD²-Router for cost-sensitive glaucoma triage. By separating deferral from expert allocation, enforcing per-sample human availability, and regularizing expert use, MPD²-Router addresses key deployment failures of standard L2D methods: indiscriminate deferral, expert collapse, asymmetric clinical harm, and distribution shift. Across three glaucoma cohorts, the proposed method improves diagnostic utility, lowers clinical and total cost, maintains controlled deferral, and yields more balanced expert utilization than strong baselines. These results support structured human–AI routing as a practical direction for safer ophthalmic AI deployment. A limitation is the scarcity of dense prospective multi-expert annotations, so our evaluation relies on retrospective cross-cohort datasets with heterogeneous and partially observed expert labels; prospective clinical validation and appropriate regulatory review remain necessary before deployment. However, this limitation reflects the real clinical setting our mask-aware formulation is designed for, and the cross-cohort results indicate that MPD²-Router remains effective under heterogeneous and sparse expert supervision.

References

- Lisa S Abrams, Ingrid U Scott, George L Spaeth, Harry A Quigley, and Rohit Varma. Agreement among optometrists, ophthalmologists, and residents in evaluating the optic disc for glaucoma. *Ophthalmology*, 101(10):1662–1667, 1994.
- Jean V Alves, Diogo Leitão, Sérgio Jesus, Marco OP Sampaio, Javier Liébana, Pedro Saleiro, Mário AT Figueiredo, and Pedro Bizarro. Cost-sensitive learning to defer to multiple experts with workload constraints. *arXiv preprint arXiv:2403.06906*, 2024.
- Yuzhou Cao, Hussein Mozannar, Lei Feng, Hongxin Wei, and Bo An. In defense of softmax parametrization for calibrated and consistent learning to defer. *Advances in Neural Information Processing Systems*, 36:38485–38503, 2023.
- Sean X Chen and Jun S Liu. Statistical applications of the poisson-binomial and conditional bernoulli distributions. *Statistica Sinica*, pages 875–892, 1997.
- Krishnamurthy Dvijotham, Jim Winkens, Melih Barsbey, Sumedh Ghaisas, Robert Stanforth, Nick Pawlowski, Patricia Strachan, Zahra Ahmed, Shekoofeh Azizi, Yoram Bachrach, et al. Enhancing the reliability and accuracy of ai-enabled diagnosis via complementarity-driven deferral to clinicians. *Nature Medicine*, 29(7):1814–1820, 2023.
- Huihui Fang, Fei Li, Junde Wu, Huazhu Fu, Xu Sun, Xingxing Cao, Jaemin Son, Shuang Yu, Menglu Zhang, Chenglang Yuan, Cheng Bian, et al. Refuge2 challenge: Treasure for multi-domain learning in glaucoma assessment. *arXiv preprint arXiv:2202.08994*, 2022.
- Paul J Foster, Ralf Buhrmann, Harry A Quigley, and Gordon J Johnson. The definition and classification of glaucoma in prevalence surveys. *British journal of ophthalmology*, 86(2):238–242, 2002.
- Yonatan Geifman and Ran El-Yaniv. Selective classification for deep neural networks. *Advances in neural information processing systems*, 30, 2017.
- Yonatan Geifman and Ran El-Yaniv. Selectivenet: A deep neural network with an integrated reject option. In *International conference on machine learning*, pages 2151–2159. PMLR, 2019.
- Chuan Guo, Geoff Pleiss, Yu Sun, and Kilian Q Weinberger. On calibration of modern neural networks. In *International conference on machine learning*, pages 1321–1330. PMLR, 2017.
- Yuki Hagiwara, Joel En Wei Koh, Jen Hong Tan, Sulatha V Bhandary, Augustinus Laude, Edward J Ciaccio, Louis Tong, and U Rajendra Acharya. Computer-aided diagnosis of glaucoma using fundus images: A review. *Computer methods and programs in biomedicine*, 165:1–12, 2018.
- Patrick Hemmer, Sebastian Schellhammer, Michael Vössing, Johannes Jakubik, and Gerhard Satzger. Forming effective human-ai teams: Building machine learning models that complement the capabilities of multiple experts. *arXiv preprint arXiv:2206.07948*, 2022.
- S Kavitha, S Karthikeyan, and K Duraiswamy. Early detection of glaucoma in retinal images using cup to disc ratio. In *2010 Second International conference on Computing, Communication and Networking Technologies*, pages 1–5. IEEE, 2010.
- Vijay Keswani, Matthew Lease, and Krishnaram Kenthapadi. Towards unbiased and accurate deferral to multiple experts. In *Proceedings of the 2021 AAAI/ACM Conference on AI, Ethics, and Society*, pages 154–165, 2021.
- Jonathan Krause, Varun Gulshan, Ehsan Rahimy, Peter Karth, Kasumi Widner, Greg S Corrado, Lily Peng, and Dale R Webster. Grader variability and the importance of reference standards for evaluating machine learning models for diabetic retinopathy. *Ophthalmology*, 125(8):1264–1272, 2018.
- JR Harish Kumar, Chandra Sekhar Seelamantula, JH Gagan, Yogish S Kamath, Neetha IR Kuzhupilly, U Vivekanand, Preeti Gupta, and Shilpa Patil. Chákṣu: A glaucoma specific fundus image database. *Scientific data*, 10(1):70, 2023.

- Ze Liu, Han Hu, Yutong Lin, Zhuliang Yao, Zhenda Xie, Yixuan Wei, Jia Ning, Yue Cao, Zheng Zhang, Li Dong, et al. Swin transformer v2: Scaling up capacity and resolution. In *Proceedings of the IEEE/CVF conference on computer vision and pattern recognition*, pages 12009–12019, 2022.
- David Madras, Toni Pitassi, and Richard Zemel. Predict responsibly: improving fairness and accuracy by learning to defer. *Advances in neural information processing systems*, 31, 2018.
- Anqi Mao, Christopher Mohri, Mehryar Mohri, and Yutao Zhong. Two-stage learning to defer with multiple experts. *Advances in neural information processing systems*, 36:3578–3606, 2023.
- Anqi Mao, Mehryar Mohri, and Yutao Zhong. Principled approaches for learning to defer with multiple experts. In *International Workshop on Combinatorial Image Analysis*, pages 107–135. Springer, 2024.
- Hussein Mozannar and David Sontag. Consistent estimators for learning to defer to an expert. In *International conference on machine learning*, pages 7076–7087. PMLR, 2020.
- Harikrishna Narasimhan, Wittawat Jitkrittum, Aditya K Menon, Ankit Rawat, and Sanjiv Kumar. Post-hoc estimators for learning to defer to an expert. *Advances in Neural Information Processing Systems*, 35:29292–29304, 2022.
- Nastaran Okati, Abir De, and Manuel Rodriguez. Differentiable learning under triage. *Advances in Neural Information Processing Systems*, 34:9140–9151, 2021.
- Maxime Oquab, Timothée Darcet, Théo Moutakanni, Huy Vo, Marc Szafraniec, Vasil Khalidov, Pierre Fernandez, Daniel Haziza, Francisco Massa, Alaaeldin El-Nouby, et al. Dinov2: Learning robust visual features without supervision. *arXiv preprint arXiv:2304.07193*, 2023.
- José Ignacio Orlando, Huazhu Fu, João Barbosa Breda, Karel Van Keer, Deepti R Bathula, Andrés Diaz-Pinto, Ruogu Fang, Pheng-Ann Heng, Jeyoung Kim, JoonHo Lee, et al. Refuge challenge: A unified framework for evaluating automated methods for glaucoma assessment from fundus photographs. *Medical image analysis*, 59:101570, 2020.
- Sayeh Pourjavan, Gen-Hua Bourguignon, Cristina Marinescu, Loic Otjacques, and Antonella Boschi. Evaluating the influence of clinical data on inter-observer variability in optic disc analysis for ai-assisted glaucoma screening. *Clinical Ophthalmology*, pages 3999–4009, 2024.
- Maithra Raghu, Katy Blumer, Greg Corrado, Jon Kleinberg, Ziad Obermeyer, and Sendhil Mullainathan. The algorithmic automation problem: Prediction, triage, and human effort. *arXiv preprint arXiv:1903.12220*, 2019.
- Marcus D Ruopp, Neil J Perkins, Brian W Whitcomb, and Enrique F Schisterman. Youden index and optimal cut-point estimated from observations affected by a lower limit of detection. *Biometrical Journal: Journal of Mathematical Methods in Biosciences*, 50(3):419–430, 2008.
- Dharmesh Tailor, Aditya Patra, Rajeev Verma, Putra Manggala, and Eric Nalisnick. Learning to defer to a population: A meta-learning approach. In *International Conference on Artificial Intelligence and Statistics*, pages 3475–3483. PMLR, 2024.
- Chin Sheng Teoh, Kah Hie Wong, Di Xiao, Hung Chew Wong, Paul Zhao, Hwei Wuen Chan, Yew Sen Yuen, Thet Naing, Kanagasingam Yogesan, and Victor Teck Chang Koh. Variability in grading diabetic retinopathy using retinal photography and its comparison with an automated deep learning diabetic retinopathy screening software. In *Healthcare*, volume 11, page 1697. MDPI, 2023.
- James M Tielsch, Joanne Katz, Harry A Quigley, Neil R Miller, and Alfred Sommer. Intraobserver and interobserver agreement in measurement of optic disc characteristics. *Ophthalmology*, 95(3): 350–356, 1988.
- Rohit Varma, William C Steinmann, and Ingrid U Scott. Expert agreement in evaluating the optic disc for glaucoma. *Ophthalmology*, 99(2):215–221, 1992.
- Rajeev Verma and Eric Nalisnick. Calibrated learning to defer with one-vs-all classifiers. In *International Conference on Machine Learning*, pages 22184–22202. PMLR, 2022.

Haoqi Wang, Zhizhong Li, Litong Feng, and Wayne Zhang. Vim: Out-of-distribution with virtual-logit matching. In *Proceedings of the IEEE/CVF conference on computer vision and pattern recognition*, pages 4921–4930, 2022.

William J Youden. Index for rating diagnostic tests. *Cancer*, 3(1):32–35, 1950.

Zhuo Zhang, Feng Shou Yin, Jiang Liu, Wing Kee Wong, Ngan Meng Tan, Beng Hai Lee, Jun Cheng, and Tien Yin Wong. Origa-light: An online retinal fundus image database for glaucoma analysis and research. In *2010 Annual international conference of the IEEE engineering in medicine and biology*, pages 3065–3068. IEEE, 2010.

Yukun Zhou, Mark A Chia, Siegfried K Wagner, Murat S Ayhan, Dominic J Williamson, Robbert R Struyven, Timing Liu, Moucheng Xu, Mateo G Lozano, Peter Woodward-Court, et al. A foundation model for generalizable disease detection from retinal images. *Nature*, 622(7981):156–163, 2023.

A Related Work

Selective prediction, algorithmic triage, and learning to defer. Learning to defer (L2D) is closely related to selective prediction and classification with a reject option, where a model abstains on uncertain inputs to improve the risk–coverage trade-off [Geifman and El-Yaniv, 2017, 2019]. However, classical selective prediction treats abstention as an unstructured reject action, whereas clinical deployment requires deciding not only whether to abstain but also whether the downstream human decision-maker is likely to improve the final outcome. This distinction motivated early human–AI triage and deferral frameworks. Madras et al. [2018] introduced learning to defer as a system-level alternative to pure automation, showing that models can improve both accuracy and fairness by passing selected cases to external decision-makers. Raghu et al. [2019] further argued that automation is not simply a question of whether an algorithm outperforms humans on average, but an instance-wise allocation problem that depends on both algorithmic and human error. Subsequent work on differentiable triage formalized this division of labor and showed that models trained for full automation may be suboptimal when only a subset of cases will be handled by the algorithm [Okati et al., 2021].

Single-expert learning to defer. A central theoretical foundation for L2D was established by Mozannar and Sontag [2020], who introduced a Bayes-consistent surrogate for single-expert deferral by casting the classify-or-defer decision as an augmented cost-sensitive classification problem. Verma and Nalisnick [2022] identified calibration limitations in the softmax-style formulation and proposed a one-vs-all (OvA) parameterization that yields calibrated estimates of expert correctness while preserving consistency. Cao et al. [2023] subsequently showed that the calibration failure is not inherent to softmax itself, but rather to symmetric surrogate design, and proposed an asymmetric softmax loss that can recover both consistency and calibrated probability estimation. In parallel, Narasimhan et al. [2022] developed post-hoc plug-in estimators that decouple base classifier training from the deferral function, which addresses underfitting caused by jointly optimizing classification and deferral under nontrivial deferral costs.

Multi-expert deferral. Extensions from a single expert to multiple experts have proceeded along several complementary axes. Keswani et al. [2021] framed multi-expert deferral as a joint classifier–allocator problem in which the system chooses among the model and multiple human experts, with an emphasis on accuracy and fairness under heterogeneous expert behavior. Hemmer et al. [2022] proposed a human–AI team formation approach that jointly learns classifier predictions and expert allocation, showing that team performance can improve when the model complements rather than duplicates human expertise. Verma and Nalisnick [2022] studied the statistical properties of multi-expert L2D, deriving consistent softmax and OvA surrogates, analyzing confidence calibration across experts, and introducing conformal expert-set selection. Mao et al. [2023] established a two-stage multi-expert L2D framework with \mathcal{H} -consistency and Bayes-consistency guarantees, where a predictor is first trained and a deferral function is then learned to assign each input to the most suitable expert. More recent theoretically grounded work has further studied surrogate design, realizable consistency, and cost-sensitive deferral in multi-expert settings [Mao et al., 2024, Alves et al., 2024]. Lastly, Taylor et al. [2024] considered learning to defer to a population of experts, using meta-learning to adapt to experts whose predictions were not observed during training.

Clinical human–AI deferral. Clinical AI provides a particularly strong motivation for L2D because both AI models and human experts are imperfect, and their errors may be complementary. In medical imaging, Complementarity-Driven Deferral to Clinical Workflow (CoDoC) showed that selective deferral between an AI model and a clinical workflow can improve diagnostic accuracy and reduce workload in screening settings [Dvijotham et al., 2023]. Ophthalmology is especially aligned with this perspective: diagnostic decisions are affected by image quality, disease severity, out-of-distribution acquisition conditions, and inter-grader variability in optic-disc assessment [Varma et al., 1992, Pourjavan et al., 2024]. These properties make glaucoma screening a natural setting for selective, cost-aware, and expert-aware routing rather than uniform automation or indiscriminate referral.

Positioning of MPD²-Router. Despite substantial progress, existing L2D methods primarily emphasize consistency, calibration, or post-hoc deferral, and most multi-expert formulations assume a fixed expert set, dense expert annotations, or an unregularized allocation over candidate experts. They provide limited machinery for handling heterogeneous expert availability masks, incorporating

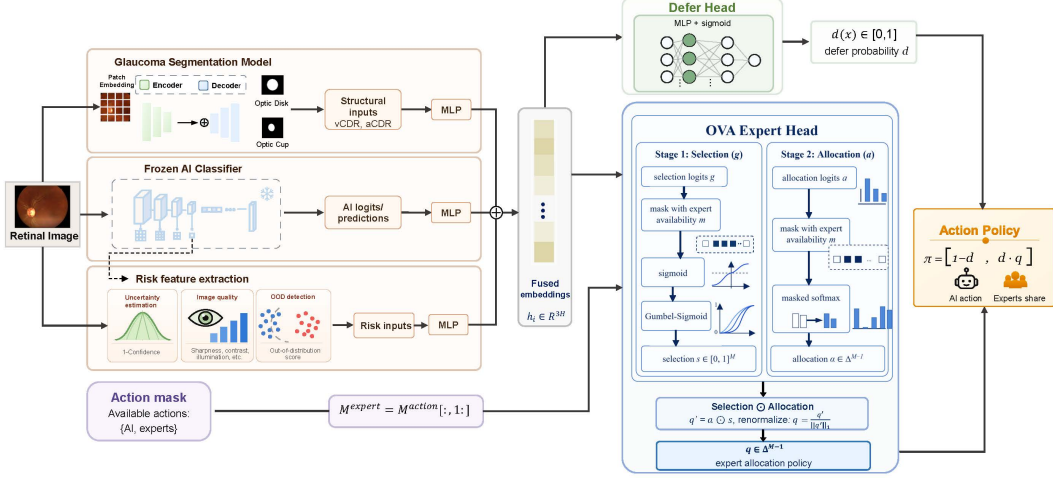


Figure 2: Overview of MPD²-Router. A retinal image is processed by three complementary branches: a frozen AI classifier for diagnostic logits, a glaucoma segmentation model for structural biomarkers such as vCDR and aCDR, and risk-feature extractors for uncertainty, image quality, and OOD signals. These signals are fused into an embedding h_i , which is passed to a dual-head router. The defer head estimates the probability d_i of human referral, while the mask-aware expert head first selects a feasible expert support and then allocates probability mass over available experts. The final policy $\pi_\theta(x_i, m_i^{\text{exp}}) = (1 - d_i, d_i q_i)$ therefore jointly determines whether the AI prediction is retained or the case is deferred to a specific human expert.

clinically-grounded priors over expert competence, controlling operational deferral rates, or preventing routing mass from collapsing onto a small subset of experts. MPD²-Router addresses these gaps through a mask-aware, prior-regularized dual-head architecture. Unlike single-softmax formulations, it explicitly separates the decision of *whether to defer* from the conditional decision of *whom to defer to*. The defer head estimates a soft human-referral probability, while the expert head performs stochastic support selection and masked allocation only over feasible experts. In addition, our method incorporates fused clinical reliability signals, including AI logits, uncertainty, image quality, OOD risk, and structural glaucoma biomarkers; uses group-specific distribution priors and rank-based JS regularization to reduce expert collapse; and enforces a soft deferral budget through an augmented Lagrangian objective. Thus, MPD²-Router *shifts multi-expert L2D from a purely accuracy-driven allocation problem toward a clinically aligned, availability-aware, cost-aware, and collapse-resistant routing framework* for robust human–AI glaucoma screening.

B Workflow and Dual-Head Architecture of MPD²-Router

Figure 2 illustrates the complete MPD²-Router workflow. Given a retinal image, the model extracts complementary diagnostic, structural, and reliability signals from a frozen AI classifier, a glaucoma segmentation model, and risk-feature modules. These signals are fused into a shared representation h_i , which feeds a dual-head routing architecture. This dual-head design separates the decision of *whether to defer* from the decision of *whom to defer to*: the defer head outputs a scalar deferral probability d_i , whereas the expert head produces a conditional, mask-aware allocation distribution q_i over only the available experts. Consequently, the final policy $\pi_\theta = (1 - d_i, d_i q_i)$ provides an interpretable and feasibility-constrained mechanism for balancing AI retention against expert-specific human referral.

C Deferred-load form of the GSDP penalty

We expand the group-specific distribution prior (GSDP) in its KL instantiation. Let

$$D_+ := \sum_{i=1}^N d_i$$

denote the total soft deferred mass, and assume $D_+ > 0$. For each group $g \in \{1, \dots, G\}$, define the group-level deferred mass and deferred expert load by

$$D_g = \sum_{i:g(i)=g} d_i, \quad Q_{g,j} = \sum_{i:g(i)=g} d_i q_{i,j}, \quad Q_g = (Q_{g,1}, \dots, Q_{g,M}).$$

Since q_i is a normalized conditional distribution over feasible experts, we have

$$\sum_{j=1}^M Q_{g,j} = \sum_{i:g(i)=g} d_i \sum_{j=1}^M q_{i,j} = D_g.$$

For every active group g with $D_g > 0$, the normalized deferred expert-load distribution is therefore

$$\tilde{q}_{g,j} = \frac{Q_{g,j}}{D_g}, \quad \sum_{j=1}^M \tilde{q}_{g,j} = 1.$$

The GSDP penalty is

$$\mathcal{L}_{\text{GSDP}}(\theta) = \sum_{g=1}^G \omega_g D(\tilde{q}_g \parallel \tilde{p}_g), \quad \omega_g = \frac{D_g}{D_+}.$$

Inactive groups with $D_g = 0$ have $\omega_g = 0$ and contribute no loss.

For the KL choice,

$$D(\tilde{q}_g \parallel \tilde{p}_g) = \sum_{j=1}^M \tilde{q}_{g,j} \log \frac{\tilde{q}_{g,j}}{\tilde{p}_{g,j}},$$

with the convention $0 \log 0 = 0$, and with the usual requirement that $\tilde{p}_{g,j} > 0$ whenever $\tilde{q}_{g,j} > 0$. Substituting $\omega_g = D_g/D_+$ and $\tilde{q}_{g,j} = Q_{g,j}/D_g$ gives

$$\mathcal{L}_{\text{GSDP}}^{\text{KL}}(\theta) = \sum_{g=1}^G \frac{D_g}{D_+} \sum_{j=1}^M \frac{Q_{g,j}}{D_g} \log \frac{Q_{g,j}/D_g}{\tilde{p}_{g,j}} \quad (7)$$

$$= \frac{1}{D_+} \sum_{g=1}^G \sum_{j=1}^M Q_{g,j} \log \frac{Q_{g,j}}{D_g \tilde{p}_{g,j}}. \quad (8)$$

Thus the KL-GSDP penalty is equivalently a normalized divergence between the actual group-wise deferred expert load Q_g and the target deferred load $D_g \tilde{p}_g$. In particular, for each group g , the target is not merely a probability vector \tilde{p}_g , but a load vector whose total mass is scaled by the amount of deferred mass assigned to that group.

Corollary 1 (KL-GSDP as load matching). *For a fixed active group g with $D_g > 0$, the KL-GSDP group term*

$$\Phi_g(Q_g) = \sum_{j=1}^M Q_{g,j} \log \frac{Q_{g,j}}{D_g \tilde{p}_{g,j}}$$

is minimized over the simplex-constrained load set

$$\mathcal{Q}_g = \left\{ Q_g \in \mathbb{R}_+^M : \sum_{j=1}^M Q_{g,j} = D_g \right\}$$

if and only if

$$Q_g = D_g \tilde{p}_g.$$

Proof. Since $D_g > 0$, write $r_g = Q_g/D_g$. Then $r_g \in \Delta^{M-1}$, and

$$\Phi_g(Q_g) = D_g \sum_{j=1}^M r_{g,j} \log \frac{r_{g,j}}{\tilde{p}_{g,j}} = D_g \text{KL}(r_g \parallel \tilde{p}_g).$$

By nonnegativity of KL divergence,

$$\Phi_g(Q_g) \geq 0,$$

with equality if and only if $r_g = \tilde{p}_g$. Therefore the unique minimizer on \mathcal{Q}_g is

$$Q_g = D_g \tilde{p}_g. \quad \square$$

D Expansion and activation property of the rank-majorization JS penalty

We give the full construction of the rank-majorization Jensen–Shannon penalty. For sample i , let

$$\mathcal{A}_i = \{j : m_{i,j}^{\text{exp}} = 1\}, \quad k_i = |\mathcal{A}_i|$$

denote the feasible expert set and its cardinality. The conditional expert allocation satisfies

$$q_i \in \Delta(\mathcal{A}_i), \quad q_{i,j} = 0 \quad \text{for } j \notin \mathcal{A}_i.$$

Let

$$q_i^\downarrow = (q_{i,(1)}, \dots, q_{i,(k_i)})$$

be the vector of feasible expert probabilities sorted in nonincreasing order, so that

$$q_{i,(1)} \geq q_{i,(2)} \geq \dots \geq q_{i,(k_i)}, \quad \sum_{\ell=1}^{k_i} q_{i,(\ell)} = 1.$$

Ties may be broken arbitrarily; the construction is permutation-invariant and is piecewise differentiable almost everywhere.

We compare this sorted allocation profile to a truncated geometric rank profile

$$g_i = (g_{i,1}, \dots, g_{i,k_i}) \in \Delta^{k_i-1},$$

defined by

$$g_{i,\ell} = \frac{\exp\{-\tau_{\text{rank}}(\ell-1)\}}{\sum_{r=1}^{k_i} \exp\{-\tau_{\text{rank}}(r-1)\}}, \quad \ell = 1, \dots, k_i,$$

where $\tau_{\text{rank}} \geq 0$ controls the concentration of the reference profile. Larger τ_{rank} permits a more top-heavy reference, whereas smaller τ_{rank} encourages a flatter allocation across available experts.

Define the cumulative rank masses

$$R_i(t) = \sum_{\ell=1}^t q_{i,(\ell)}, \quad G_i(t) = \sum_{\ell=1}^t g_{i,\ell}, \quad t = 1, \dots, k_i.$$

Since both q_i^\downarrow and g_i are probability vectors,

$$R_i(k_i) = G_i(k_i) = 1.$$

Thus, only strict prefix inequalities $t < k_i$ can reveal excessive concentration.

We define the margin-violation score

$$v_i = \max_{1 \leq t \leq k_i} [R_i(t) - G_i(t) - m]_+,$$

where $m \geq 0$ is a slack margin and $[x]_+ = \max\{x, 0\}$. The corresponding activation variable is

$$\chi_i = \mathbf{1}[v_i > 0].$$

Equivalently,

$$\chi_i = 1 \iff \exists t \in \{1, \dots, k_i\} \text{ such that } R_i(t) > G_i(t) + m.$$

Therefore, the rank penalty is activated only when the sorted router allocation places more mass in its leading ranks than the geometric reference allows up to margin m .

For the active samples, we penalize the Jensen–Shannon divergence between the sorted allocation profile and the geometric reference profile:

$$\text{JS}(q_i^\downarrow \| g_i) = \frac{1}{2} \text{KL}(q_i^\downarrow \| s_i) + \frac{1}{2} \text{KL}(g_i \| s_i), \quad s_i = \frac{1}{2}(q_i^\downarrow + g_i).$$

Expanding the KL terms gives

$$\text{JS}(q_i^\downarrow \| g_i) = \frac{1}{2} \sum_{\ell=1}^{k_i} q_{i,(\ell)} \log \frac{2q_{i,(\ell)}}{q_{i,(\ell)} + g_{i,\ell}} + \frac{1}{2} \sum_{\ell=1}^{k_i} g_{i,\ell} \log \frac{2g_{i,\ell}}{q_{i,(\ell)} + g_{i,\ell}}.$$

The rank-majorization JS penalty is then

$$\mathcal{L}_{\text{rankJS}}(\theta) = \frac{1}{\sum_{i=1}^N d_i} \sum_{i=1}^N d_i \chi_i \text{JS}(q_i^\downarrow \| g_i).$$

Thus, the penalty acts only on samples that are softly deferred and whose conditional expert allocation is more top-heavy than the allowed geometric reference profile.

Proposition 1 (Activation criterion of the rank-majorization penalty). *For sample i , suppose that*

$$R_i(t) \leq G_i(t) + m \quad \text{for all } t = 1, \dots, k_i.$$

Then $\chi_i = 0$, and sample i contributes no rank-majorization JS penalty. Conversely, if $\chi_i = 1$, then there exists a prefix rank $t < k_i$ such that

$$R_i(t) > G_i(t) + m,$$

meaning that the routed expert distribution assigns excessive cumulative mass to its top-ranked experts relative to the geometric reference profile.

Proof. By definition,

$$v_i = \max_{1 \leq t \leq k_i} [R_i(t) - G_i(t) - m]_+, \quad \chi_i = \mathbf{1}[v_i > 0].$$

If

$$R_i(t) \leq G_i(t) + m \quad \forall t = 1, \dots, k_i,$$

then

$$R_i(t) - G_i(t) - m \leq 0 \quad \forall t = 1, \dots, k_i.$$

Therefore,

$$[R_i(t) - G_i(t) - m]_+ = 0 \quad \forall t,$$

and hence

$$v_i = 0.$$

It follows immediately that

$$\chi_i = \mathbf{1}[v_i > 0] = 0.$$

The sample-level contribution to the rank-majorization JS penalty is

$$d_i \chi_i \text{JS}(q_i^\downarrow \| g_i),$$

which is zero whenever $\chi_i = 0$. Thus, sample i contributes no rank penalty.

Conversely, suppose $\chi_i = 1$. Then $v_i > 0$. By the definition of v_i , there must exist at least one rank prefix $t \in \{1, \dots, k_i\}$ such that

$$[R_i(t) - G_i(t) - m]_+ > 0.$$

This is equivalent to

$$R_i(t) - G_i(t) - m > 0,$$

or

$$R_i(t) > G_i(t) + m.$$

Because both q_i^\downarrow and g_i are probability vectors,

$$R_i(k_i) = G_i(k_i) = 1.$$

For $m \geq 0$, the inequality

$$R_i(k_i) > G_i(k_i) + m$$

cannot hold, since it would require

$$1 > 1 + m.$$

Therefore, any activating violation must occur at a strict prefix $t < k_i$. Hence $\chi_i = 1$ only when the sorted router allocation places more mass in its top t experts than the geometric reference profile allows, up to margin m . This is precisely the sense in which the penalty is activated only by excessively top-heavy expert allocation. \square

E Pseudo Labeling

We use three public glaucoma fundus-image cohorts with complementary annotation patterns. REFUGE is a Chinese retinal fundus glaucoma benchmark with clinical glaucoma labels and optic-disc/optic-cup annotations from seven expert ophthalmologists, but without dense per-expert diagnostic decisions [Orlando et al., 2020]. CHAKSU is an Indian-ethnicity glaucoma dataset acquired using multiple fundus cameras and provides optic-disc/optic-cup contours together with binary glaucoma decisions from five expert ophthalmologists [Kumar et al., 2023]. ORIGA is a Singaporean fundus-image dataset with image-level glaucoma labels and optic-disc/optic-cup annotations, but without the multi-expert decision structure needed for expert-routing supervision [Zhang et al., 2010]. Because these cohorts differ in acquisition devices, population characteristics, annotation protocols, and image quality, they provide a natural setting for studying expert routing under heterogeneous supervision and distribution shift.

E.1 REFUGE semi-synthetic label generation

For REFUGE, structural annotations are available, but dense per-expert decisions are incomplete. We therefore generate semi-synthetic per-expert outcomes from annotated optic-disc and optic-cup geometry. This construction is motivated by the clinical role of optic-nerve-head morphology in glaucoma assessment: vertical cup-to-disc ratio (vCDR) is a widely used and relatively robust index of glaucomatous neuroretinal rim loss, and cup-to-disc measurements are commonly used in glaucoma screening and diagnosis [Foster et al., 2002, Kavitha et al., 2010, Hagiwara et al., 2018]. We treat the generated labels as noisy semi-synthetic supervision rather than true expert annotations.

Geometric biomarker extraction. For case i and expert/annotator j , let the fitted optic-disc and optic-cup ellipses be

$$e_{ij}^D = (w_{ij}^D, h_{ij}^D, \theta_{ij}^D, c_{x,ij}^D, c_{y,ij}^D), \quad e_{ij}^C = (w_{ij}^C, h_{ij}^C, \theta_{ij}^C, c_{x,ij}^C, c_{y,ij}^C).$$

For an ellipse with width w , height h , and rotation angle θ , let $a = w/2$ and $b = h/2$ denote the semi-major and semi-minor axes. We define the vertical diameter functional

$$\text{VD}(w, h, \theta) = 2\sqrt{a^2 \sin^2 \theta + b^2 \cos^2 \theta}.$$

Set

$$\text{VD}_{ij}^D = \text{VD}(w_{ij}^D, h_{ij}^D, \theta_{ij}^D), \quad \text{VD}_{ij}^C = \text{VD}(w_{ij}^C, h_{ij}^C, \theta_{ij}^C).$$

We then compute three structural biomarkers:

$$\text{vCDR}_{ij} = \frac{\text{VD}_{ij}^C}{\text{VD}_{ij}^D}, \quad \text{aCDR}_{ij} = \frac{a_{ij}^C b_{ij}^C}{a_{ij}^D b_{ij}^D}, \quad \text{dec}_{ij} = \frac{\|(c_{x,ij}^C, c_{y,ij}^C) - (c_{x,ij}^D, c_{y,ij}^D)\|_2}{\text{VD}_{ij}^D}.$$

Here, vCDR_{ij} measures vertical cup enlargement, aCDR_{ij} measures relative cup area, and dec_{ij} captures cup-disc decentration. These quantities summarize clinically meaningful optic-nerve-head structure while remaining simple enough to support interpretable semi-synthetic label generation.

We define the geometry feature vector

$$\phi_{ij} = \begin{bmatrix} 1 \\ \text{vCDR}_{ij} \\ \text{aCDR}_{ij} \\ \log(\text{VD}_{ij}^D) \\ \text{dec}_{ij} \end{bmatrix}.$$

For each expert j , we fit a logistic model mapping geometry to a glaucoma evidence score:

$$s_{ij} = w_j^\top \phi_{ij}, \quad p_{ij}^{\text{raw}} = \sigma(s_{ij}), \quad \sigma(t) = \frac{1}{1 + \exp(-t)}, \quad (9)$$

where w_j is estimated by maximum likelihood on the training split \mathcal{D}_{tr} . All fitting and calibration are performed using training/calibration data only to avoid test-set leakage.

Per-expert temperature calibration. Because the raw logistic scores may be over- or under-confident, we calibrate each expert-specific score using temperature scaling [Guo et al., 2017]:

$$p_{ij}^{\text{cal}} = \sigma\left(\frac{s_{ij}}{T_j}\right), \quad T_j > 0. \quad (10)$$

The temperature T_j is selected on a held-out calibration split \mathcal{D}_{cal} by minimizing negative log-likelihood. Calibration quality is then evaluated on the test split \mathcal{D}_{te} .

Geometry-only case difficulty. Let $\text{vCDR}_i^{\text{med}}$ denote the median vCDR across available annotations for case i . We define a geometry-only difficulty score

$$\beta_i = \exp\left(-\kappa \left| \text{vCDR}_i^{\text{med}} - \tau \right| \right), \quad \kappa > 0. \quad (11)$$

The threshold τ is chosen as the vCDR cutoff that maximizes the Youden index on the training data, a standard criterion for selecting diagnostic operating points from ROC analysis [Youden, 1950, Ruopp et al., 2008]. Thus, anatomically borderline cases near τ receive larger β_i , reflecting greater ambiguity in geometry-based diagnosis.

Case-specific operating point. Given expert-level baseline operating characteristics $(\text{Se}_j, \text{Sp}_j)$, we construct case-specific sensitivity and specificity as

$$\text{logit}(\text{Se}_{ij}) = \text{logit}(\text{Se}_j) + \alpha_j (p_{ij}^{\text{cal}} - \rho) - b\beta_i, \quad (12)$$

$$\text{logit}(\text{Sp}_{ij}) = \text{logit}(\text{Sp}_j) - \gamma_j (p_{ij}^{\text{cal}} - \rho) - d\beta_i, \quad (13)$$

where $\alpha_j, \gamma_j \geq 0$ control how strongly calibrated structural evidence changes the expert operating point, $b, d \geq 0$ penalize borderline cases, and ρ is a reference evidence level. This construction allows expert performance to vary with case morphology while preserving each expert’s baseline sensitivity–specificity profile.

Poisson–binomial sampling with correctness constraints. Let $c_{ij} \in \{0, 1\}$ indicate whether expert j is correct on case i :

$$c_{ij} = \mathbf{1}\{\hat{y}_{ij} = y_i\}.$$

Conditioned on the true label and geometry, we model correctness as

$$c_{ij} \mid (y_i, \phi_{ij}) \sim \text{Bernoulli}(\Phi_{ij}), \quad \Phi_{ij} = y_i \text{Se}_{ij} + (1 - y_i) \text{Sp}_{ij}. \quad (14)$$

The number of correct experts,

$$K_i = \sum_{j=1}^J c_{ij},$$

therefore follows a Poisson–binomial distribution because it is the sum of independent Bernoulli variables with non-identical success probabilities [Chen and Liu, 1997]. To avoid unrealistically poor synthetic expert panels, we condition on a minimum quality constraint $K_i \geq k_{\text{min}}$, yielding a conditional Bernoulli law.

We sample exactly under this constraint using a dynamic program. Define suffix probabilities

$$q_j(s) = \Pr\left(\sum_{t=j}^J c_{it} = s \mid y_i, \phi_{i1:J}\right),$$

with boundary conditions $q_{J+1}(0) = 1$ and $q_{J+1}(s > 0) = 0$. The recursion is

$$q_j(s) = (1 - \Phi_{ij})q_{j+1}(s) + \Phi_{ij}q_{j+1}(s - 1), \quad s \geq 0.$$

We first draw

$$K_i \sim \Pr(K_i = k \mid K_i \geq k_{\text{min}}) = \frac{q_1(k)}{Z_i}, \quad k \in \{k_{\text{min}}, \dots, J\},$$

where

$$Z_i = \sum_{u=k_{\text{min}}}^J q_1(u).$$

Given the sampled total number of correct experts, we sequentially sample (c_{i1}, \dots, c_{iJ}) using

$$\Pr \left(c_{ij} = 1 \mid \sum_{t=j}^J c_{it} = r \right) = \frac{\Phi_{ij} q_{j+1}(r-1)}{q_j(r)}. \quad (15)$$

Finally, we instantiate the semi-synthetic expert label as

$$\hat{y}_{ij} = \begin{cases} y_i, & c_{ij} = 1, \\ 1 - y_i, & c_{ij} = 0, \end{cases} \quad \text{so that} \quad \Pr(\hat{y}_{ij} = 1 \mid y_i, \phi_{ij}) = y_i \Phi_{ij} + (1 - y_i)(1 - \Phi_{ij}). \quad (16)$$

This procedure produces expert-specific labels that are tied to clinically interpretable optic-disc and optic-cup morphology, preserve heterogeneous expert operating characteristics, and enforce a weak panel-quality constraint without assuming that all experts are equally reliable.

E.2 ORIGA synthetic label generation

ORIGA does not provide multi-expert annotations. We therefore induce plausible expert outcomes by retrieving morphologically similar labeled cases from REFUGE and CHAKSU in a pretrained retinal representation space. This procedure follows the intuition of case-based ophthalmic decision support, where visually similar fundus images serve as reference cases for diagnosis, while the retrieved labels are treated as noisy pseudo-supervision rather than ground-truth expert labels.

For each image, we extract embeddings using DINOv2 Oquab et al. [2023] and RETFound-MAE Zhou et al. [2023] after cropping the retinal region, followed by ℓ_2 normalization so that dot-product similarity approximates cosine similarity. For an ORIGA query image, we restrict the retrieval pool by its ground-truth class: ORIGA images with $y = 1$ are matched only to REFUGE/CHAKSU cases with $y = 1$, and ORIGA images with $y = 0$ are matched only to REFUGE/CHAKSU cases with $y = 0$. Within this label-matched pool, we compute similarity between the ORIGA embedding and all candidate embeddings, retrieve the most similar cases, fuse DINOv2 and RETFound-MAE similarity scores after per-query normalization, and retain the top seven nearest neighbors. The synthetic expert outcomes for the ORIGA image are then obtained from the retrieved neighbors’ expert labels, \hat{y}^{exp} , and used as pseudo-annotations.

We use cropped rather than uncropped fundus images because the cropped retinal region better emphasizes clinically relevant morphology, including optic-disc and cup-related structure. Moreover, this assumption is consistent with our risk-stratified analysis in Figure 1, where model-reliability risk primarily degrades the frozen AI model, whereas structural glaucoma risk, reflected by features such as aCDR and vCDR, is a more clinically meaningful source of case difficulty. Thus, similarity search in a cropped retinal representation space is intended to retrieve reference cases with comparable structural appearance rather than merely similar global image context. The resulting ORIGA pseudo-labels remain sparse: the top retrieved neighbors may contain repeated labels from the same expert, and not every expert is represented for every ORIGA case. This sparsity is desirable for our setting because it preserves the heterogeneous and incomplete expert-availability structure that the proposed mask-aware router is designed to handle.

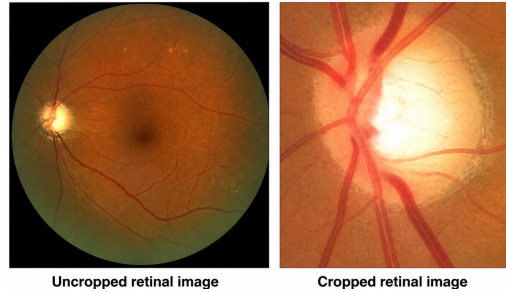


Figure 3: Retinal-region cropping used before similarity-based retrieval.

F Experiment implementation details

This section provides the implementation details required to reproduce the main experimental results, including the fixed data split, decision-time features, action masks, optimization procedure, hyperparameter selection protocol, baseline adaptations, test-time evaluation, and computational resources. All methods are trained, selected, and evaluated under the same protocol unless explicitly stated otherwise.

Table 4: Fixed train/validation/test split used for all methods. The same split is used for MPD²-Router and every baseline. Counts are reported by cohort.

Split	REFUGE	CHAKSU	ORIGA	Total
Train	400	686	325	1411
Validation	400	323	162	885
Test	400	336	163	899

F.1 Data splits and leakage control

All experiments use a fixed train/validation/test split constructed before model comparison. The split contains 3195 retinal fundus cases from REFUGE, CHAKSU, and ORIGA. The training split is used for fitting model parameters, constructing train-only priors, estimating any feature-normalization statistics, and fitting any auxiliary components required by the router. The validation split is used only for early stopping, hyperparameter selection, pruning, and model selection. The test split is held out until final evaluation and is not used for hyperparameter search, prior construction, threshold selection, or early stopping.

The frozen diagnostic backbone is trained only on the designated training data and is not updated during router training. All downstream routing methods therefore operate on the same frozen decision-time state rather than on raw images. Any statistics used to normalize continuous routing features are estimated on the training split and then applied unchanged to validation and test. Similarly, the group-specific distribution priors used by MPD²-Router are constructed from the training split only and are frozen during validation and test evaluation.

F.2 Decision-time state and masked action space

To ensure a fair comparison, every method receives the same decision-time feature vector:

$$z_i = [\text{prob}_1, \text{logit}_0, \text{logit}_1, \text{vim_risk}_z, \text{quality_risk}, \text{uncertainty}, \text{vCDR}, \text{aCDR}]_i.$$

These features summarize the frozen AI classifier output, model uncertainty, OOD risk, image-quality risk, and structural glaucoma biomarkers. The router therefore compares methods in the clinically relevant downstream decision space, rather than giving MPD²-Router privileged access to additional image information.

The unified action space contains the AI action and $M = 12$ human-expert actions. The AI action is always feasible. Human-expert feasibility is sample-specific and is encoded by the binary expert mask $m_i^{\text{exp}} \in \{0, 1\}^M$. The full action mask is

$$m_i^{\text{act}} = [1, (m_i^{\text{exp}})_1, \dots, (m_i^{\text{exp}})_M].$$

Unavailable experts are masked at both training and inference time. Thus no method can route a case to an expert whose label is unavailable for that case.

For MPD²-Router, the defer head outputs a soft deferral mass $d_i \in (0, 1)$ and the expert-allocation head outputs a conditional distribution q_i over feasible experts. The conditional expert allocation is

$$q_{i,j} = \frac{a_{i,j} s_{i,j}^{\sharp}}{\sum_{k=1}^M a_{i,k} s_{i,k}^{\sharp}}, \quad j = 1, \dots, M, \quad (17)$$

where a_i is the masked allocation distribution and s_i^{\sharp} is the repaired stochastic expert-support vector. The denominator is clamped by $\varepsilon = [\text{e.g.}, 10^{-8}]$ for numerical stability. The full action policy is

$$\tilde{\pi}_i = [1 - d_i, d_i q_{i,1}, \dots, d_i q_{i,M}].$$

As a final safety layer, we apply the masked-simplex projection

$$\Pi_{\Delta(m)}(v) = \frac{v \odot m}{\langle \mathbf{1}, v \odot m \rangle},$$

which is well-defined whenever at least one feasible action is present, and set

$$\pi_i = \Pi_{\Delta(m_i^{\text{act}})}(\tilde{\pi}_i).$$

This guarantees that the final policy places zero probability on unavailable actions.

Table 5: Training and model-selection details for MPD²-Router. Hyperparameters marked as validation-selected are chosen by the adaptive fine-tuning protocol and are reported in the released experiment configuration files.

Item	Setting
Framework	PyTorch
Optimizer	AdamW
Learning rate	validation-selected
Weight decay	10^{-4} for router parameters
Batch size	64
Maximum epochs	150
Warmup epochs	validation-selected
Early-stopping patience	18 validation epochs
Clinical costs	$c_{\text{fn}} = 2.0$, $c_{\text{fp}} = 1.5$
Prior badness costs	$c_{\text{fn}}^{\text{prior}} = 1.8$, $c_{\text{fp}}^{\text{prior}} = 1.2$
Tier-cost weight γ	validation-selected
GSDP / rank-JS weights	validation-selected
Augmented-Lagrangian parameters	validation-selected
Feature normalization	train-split statistics only
Checkpoint selection	best validation selection score after warmup
Test evaluation	held-out test split, evaluated once after selection
Random seeds	main repeated-seed experiments use 42–52

F.3 Training objective and optimization

MPD²-Router is trained to minimize the clinical–operational deployment objective directly, rather than a per-action correctness target. For sample i , the clinical cost of retaining the frozen AI model is

$$C_i^{\text{ai}} = c_{\text{fn}} y_i (1 - p_i^{\text{ai}}) + c_{\text{fp}} (1 - y_i) p_i^{\text{ai}},$$

where p_i^{ai} is the frozen AI probability for glaucoma. The clinical cost of expert j is

$$C_{i,j}^{\text{exp}} = c_{\text{fn}} \mathbf{1}[y_i = 1, \hat{y}_{i,j} = 0] + c_{\text{fp}} \mathbf{1}[y_i = 0, \hat{y}_{i,j} = 1].$$

Unless otherwise stated, we use asymmetric clinical costs $c_{\text{fn}} = 2.0$ and $c_{\text{fp}} = 1.5$, reflecting the higher clinical penalty of missed glaucoma relative to false referral.

The clinical–operational routing loss is

$$\mathcal{L}_{\text{cost}}(\theta) = \frac{1}{N} \sum_{i=1}^N \left[C_i^{\text{ai}} + d_i \left(\sum_{j=1}^M q_{i,j} (C_{i,j}^{\text{exp}} + \gamma \kappa_j) - C_i^{\text{ai}} \right) \right],$$

where d_i is the soft deferral mass, $q_{i,j}$ is the conditional expert allocation probability, κ_j is the expert-tier cost, and γ controls the contribution of operational expert cost. The full objective is

$$\mathcal{J}(\theta) = \mathcal{L}_{\text{cost}}(\theta) + w_{\text{GSDP}} \mathcal{L}_{\text{GSDP}}(\theta) + w_{\text{rank}} \mathcal{L}_{\text{rank}}(\theta) + P_{\text{AL}}(\bar{d}), \quad \bar{d} = \frac{1}{N} \sum_{i=1}^N d_i.$$

Here $\mathcal{L}_{\text{GSDP}}$ is the group-specific distribution-prior regularizer, $\mathcal{L}_{\text{rank}}$ is the rank-majorization JS regularizer, and P_{AL} is the augmented-Lagrangian penalty for the soft deferral-budget constraint.

Models are optimized with mini-batch AdamW. Feature normalization statistics are computed on the training split only and reused for validation and test. Validation performance is evaluated after each epoch, and the best validation checkpoint after the warmup period is restored before final evaluation. Hyperparameters are selected only on the validation split using the adaptive fine-tuning protocol in Section F.4. The held-out test set is evaluated once after model and hyperparameter selection; no test-set information is used for training, pruning, hyperparameter optimization, or checkpoint selection. The implementation details needed to reproduce the training protocol are summarized in Table 5; exact resolved configurations are provided in the released experiment files.

F.4 Adaptive fine-tuning and hyperparameter selection

We implement adaptive fine-tuning as a lightweight Optuna-based hyperparameter optimization loop around MPD²-Router training. Each trial samples a candidate configuration, maps it to the router’s

optimization, prior-regularization, and augmented-Lagrangian settings, and trains the model with validation-based early stopping and Hyperband pruning. The held-out test set is never used during hyperparameter search or checkpoint selection.

The search space is 16-dimensional and covers the optimizer, deferral-cost weighting, prior construction, anti-collapse regularization, and constraint control:

`lr`, `warmup_epochs`, `gamma_tier`, `tau_bad`, `w_gsdp`, `w_rank_js`,
`global_uniform_mix`, `family_uniform_mix`, `group_uniform_mix`, `family_n0`, `group_n0`,
`global_mix`, `clip_ceiling`, `clip_slack`, `al_mu`, `al_lr_lambda`.

The geometric clipping anchors are not tuned separately; they are derived from `clip_ceiling` and `clip_slack` through the support-size cap

$$\text{clip_max}(k) = \min(\text{clip_ceiling}, g_{k,1}(\rho_k) + \text{clip_slack}).$$

Adaptive HPO protocol. We use a multivariate Tree-structured Parzen Estimator (TPE) sampler with group-based conditional sampling. A hand-tuned configuration is enqueued as the first trial to seed the search, followed by 10 random startup trials before TPE acquisition is used. Hyperband pruning is applied with the minimum and maximum resources tied to the warmup epoch count and the maximum training budget, respectively, and reduction factor 3. Unless otherwise stated, each study uses 80 Optuna trials.

Within each trial, pruning and early stopping are driven by the constraint-aware validation score

$$\text{es_base} + 10 \text{ es_violation},$$

where `es_violation` measures soft deferral-budget violation. The best validation checkpoint under this rule is restored before trial evaluation. The outer Optuna objective uses an augmented Tchebycheff scalarization over clinical loss, $-MCC$, $-AUPRC$, soft tier cost, and constraint violation, relative to an EMA-updated utopia reference. We use weights (0.35, 0.15, 0.10, 0.05, 0.05) and augmentation coefficient $\rho = 0.05$. Trials producing NaN losses or metrics are pruned automatically.

After the search terminates, the selected configuration is retrained with an extended budget using the same constraint-aware validation-selection rule and is evaluated once on the held-out test set. Despite the breadth of the search space, the procedure is computationally lightweight: each trial takes approximately 2.5 minutes on the compute worker.

F.5 Baseline implementation and fairness

All baselines are evaluated on the same fixed train/validation/test split, the same decision-time state z_i , and the same masked sparse action space. Unavailable experts are masked during training and inference whenever the baseline formulation permits masking. When a method was originally designed for a different action structure, we use the closest masked sparse adaptation needed to make action-level comparison meaningful.

This benchmark is deliberately favorable to the baselines in two ways. First, all methods route from a highly informative downstream state derived from the frozen AI model, uncertainty/OOD pipeline, image-quality signal, and structural glaucoma biomarkers. Second, in the benchmark configuration, `selection_metric` is set to "surrogate" while `cost_aware_inference` is enabled. Therefore, several baselines retain their original surrogate-style training objectives while also benefiting from cost-aware routing at inference time.

The baseline adaptations are as follows. Verma-OvA is trained against per-action correctness targets under the feasible action mask. Narasimhan-PH fits separate predictors for AI correctness and expert correctness and then applies cost-aware score adjustment during routing. Mao-TwoStage uses a score-based surrogate constructed from AI correctness and expert correctness, with optional base-cost terms. Hemmer-MoE is trained with true expert labels inside a masked team cross-entropy over the classifier and available experts. Keswani et al. is included as a committee-based multi-expert collaboration baseline. Because its native formulation produces a weighted committee rather than a single routed action, we evaluate a masked top-1 projection for action-level comparisons.

Although the task label is a single binary label y_i , several baselines are trained using derived per-action correctness patterns such as "AI wrong, expert 1 correct, expert 2 wrong, expert 3 unavailable."

These targets are substantially closer to the routing answer than ordinary binary classification. In contrast, MPD²-Router is not trained to output a per-action correctness vector. It directly optimizes the clinical–operational routing objective and learns when to retain the AI, when to defer, and which feasible expert to select under asymmetric clinical cost, expert-tier cost, availability masks, and deferral-budget constraints.

F.6 Test-time evaluation

After validation-based model selection, each method is evaluated on the held-out test split. Unless explicitly stated otherwise, soft policies are converted to hard actions by masked argmax:

$$\hat{a}_i = \arg \max_{a \in \mathcal{A}_i} \pi_{i,a}.$$

If \hat{a}_i is the AI action, the final prediction is the frozen AI prediction. If \hat{a}_i is a human-expert action, the final prediction is the selected expert’s label. Because all policies are projected onto the masked simplex, test routing cannot select unavailable experts.

We report standard diagnostic metrics, including accuracy, precision, recall, specificity, F1, and MCC. We also report clinical cost, expert cost, total cost, deferral rate, deferral-budget violation, and expert-utilization statistics. Expert-collapse diagnostics are computed on the human-routed subset and include MaxShare, entropy-based effective number of experts, and normalized Gini. Cost–performance trade-off figures use the same held-out test predictions and the same cost definitions for all methods.

When results are averaged across random seeds, we report mean and standard deviation over 10 random seeds. When a single run is reported, the selected seed is fixed before test evaluation and all methods use the same seed where applicable.

F.7 Computational resources and runtime

All routing experiments are lightweight and can be reproduced without distributed training. Experiments are run on a single compute worker with a 13th-generation Intel Core i9-13905H CPU (14 physical / 20 logical cores), an NVIDIA GeForce RTX 4060 Laptop GPU (compute capability 8.9) with 8 GiB GPU memory, and 32 GiB system memory. The operating system is Windows 11, and the main software stack is Python 3.12, PyTorch 2.10 (CUDA 12.8 build), Optuna 4.8, NumPy 2.4, and scikit-learn 1.8.

The routing models are small because they operate on an eight-dimensional decision-time state rather than full images. Consequently, the dominant runtime comes from repeated validation-based hyperparameter search rather than from a single training run. Hyperband pruning further reduces wasted computation by terminating weak configurations early. In practice, each adaptive fine-tuning trial takes approximately 2.5 minutes, making it feasible to run many trials and select robust configurations without large-scale compute.

G Experiment results

G.1 AI-retention safety under distribution shift

Table 6 shows that MPD²-Router improves AI-retention safety by becoming increasingly selective under distribution shift. An effective router should retain a nontrivial AI share while keeping retained-AI accuracy high and clinical cost low. On in-distribution REFUGE, the frozen classifier is already reliable, yet MPD²-Router still preserves an autonomous share of 0.755 with near-perfect retained-AI accuracy and low clinical cost. When OOD shift, AI-only inference becomes unsafe: clinical cost grows from 0.179 (REFUGE) to 0.408 (CHAKSU) and 0.773 (ORIGA). Baseline routers exhibit two opposing failure modes, retaining a large AI share at high cost or reducing retained-AI error only through aggressive deferral that leaves few cases to the AI. MPD²-Router instead occupies a more Pareto-favorable region of the coverage–risk trade-off: on far-OOD ORIGA, it retains 20.2% of cases with 100% retained-AI accuracy and zero clinical cost, avoiding Hemmer-MoE’s overly conservative 10.4% retention. These results indicate MPD²-Router’s selective routing rather than uniform abstention or indiscriminate deferral.

Table 6: AI-retained subset performance under distribution shift. *Share* = fraction of cases kept under autonomous AI prediction; *Acc*, *MCC*, and *CC* (ClinicalCost) are computed on the retained subset. *CC* is the only minimization target (\downarrow); others maximize (\uparrow). Test set sizes: REFUGE $n=400$, CHAKSU $n=336$, ORIGA $n=163$.

Method	REFUGE				CHAKSU				ORIGA			
	Share	Acc	MCC	CC	Share	Acc	MCC	CC	Share	Acc	MCC	CC
AI-Only	1.000	0.883	0.610	0.179	1.000	0.732	0.455	0.408	1.000	0.491	0.263	0.773
Mao-TwoStage	0.780	0.997	0.962	0.006	0.530	0.978	0.343	0.042	0.288	0.915	0.753	0.138
Narasimhan	0.820	0.997	0.976	0.006	0.530	0.983	0.496	0.034	0.270	0.909	0.694	0.159
Verma-OvA	0.403	1.000	1.000	0.000	0.134	0.978	0.000	0.044	0.129	0.857	0.000	0.286
Hemmer-MoE	0.535	1.000	1.000	0.000	0.313	0.990	0.000	0.019	0.104	1.000	0.000	0.000
Keswani	0.890	0.961	0.771	0.077	0.134	1.000	0.000	0.000	0.472	0.818	0.319	0.364
MPD²-Router	0.755	0.997	0.941	0.007	0.509	0.982	0.000	0.035	0.202	1.000	0.000	0.000

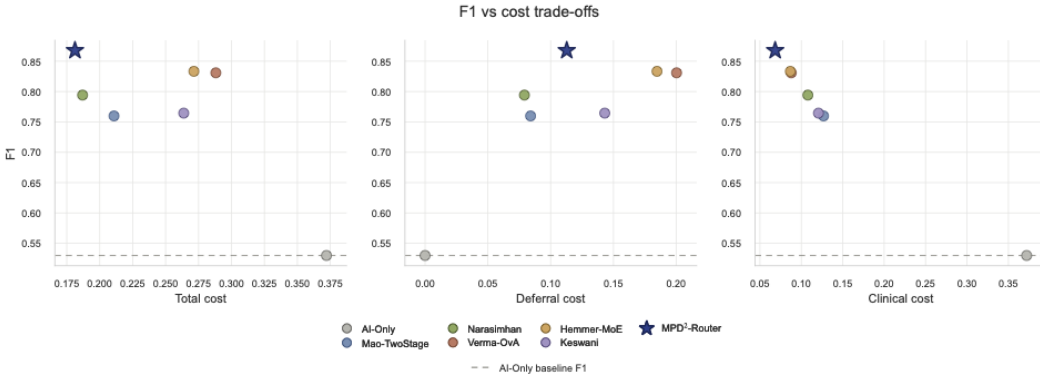


Figure 4: F1 versus total, deferral, and clinical cost. MPD²-Router lies in the upper-left region of the trade-off space, indicating a Pareto-favorable operating point: it achieves the highest F1 while maintaining the lowest total and clinical cost among the compared methods.

G.2 Cost–performance trade-off analysis

Figures 4 and 5 evaluate whether performance gains are achieved at a clinically and operationally acceptable cost. MPD²-Router consistently occupies the upper-left region of the trade-off space, achieving the highest F1 and MCC while also attaining the lowest total and clinical costs among the compared learned routing methods. AI-Only has zero deferral cost but substantially worse F1/MCC and much higher clinical cost, indicating that avoiding deferral is not clinically safe. Conversely, several baselines improve predictive performance through more expensive or less selective deferral, particularly Hemmer-MoE and Verma-OvA, which incur substantially higher total and deferral costs. These results show that MPD²-Router does not merely buy accuracy through excessive referral; instead, it learns a selective routing policy that improves diagnostic performance while reducing clinical harm and maintaining a favorable operational cost profile.

G.3 Expert performance heterogeneity and selective deferral

Motivation and matched-subset protocol. A central premise of MPD²-Router is that human readers are not interchangeable deferral targets. This assumption is clinically realistic in glaucoma screening: optic-disc assessment is known to exhibit substantial inter-observer variability, with readers differing in cup-to-disc estimation, glaucomatous-damage judgment, and sensitivity–specificity operating points [Tielsch et al., 1988, Varma et al., 1992, Abrams et al., 1994, Pourjavan et al., 2024]. We therefore evaluate each expert only on the matched subset of test vcases for which that expert provides a label. Formally, for expert j , evaluation is restricted to $\mathcal{I}_j = \{i : m_{i,j} = 1\}$, and MPD²-Router is evaluated on the same \mathcal{I}_j . This controls for the heterogeneous availability mask and ensures that the comparison measures routing quality rather than differences in case exposure.

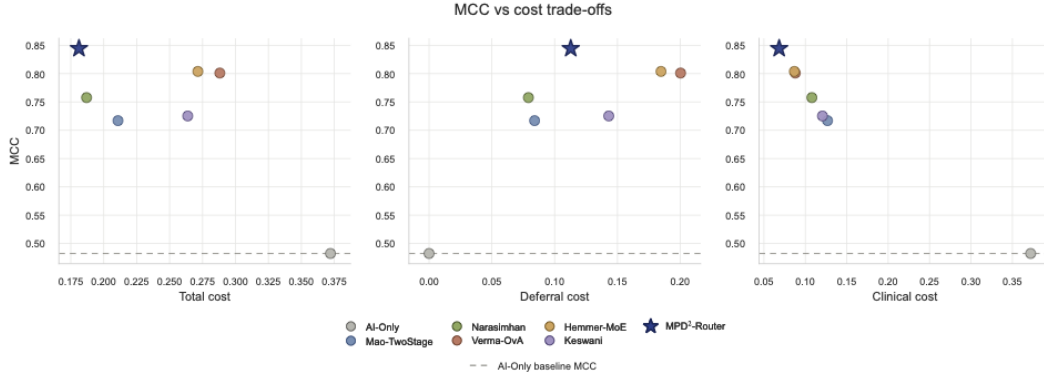


Figure 5: MCC versus total, deferral, and clinical cost. MPD²-Router again occupies the Pareto-favorable region, achieving the strongest correlation-based classification performance without requiring the high deferral costs incurred by more defer-heavy baselines.

Table 7: Per-expert performance on matched availability subsets. Sensitivity, specificity, FN/FP counts, and clinical cost are reported alongside summary metrics to expose operating-point heterogeneity that F_1 alone obscures. *Best-oracle* is the per-case selection of any reader producing the correct label and represents the achievable cohort skyline. Within each cohort, rows are sorted by F_1 .

Expert	n	Acc	Sens	Spec	F_1	MCC	FN	FP	Clin. cost
<i>Best-oracle</i>	899	1.000	1.000	1.000	1.000	1.000	0	0	0.000
<i>CHAKSU readers</i>									
chaksu_expert_1	415	0.947	0.921	0.953	0.864	0.834	6	16	0.087
chaksu_expert_3	412	0.917	0.859	0.928	0.764	0.721	9	25	0.135
chaksu_expert_4	403	0.881	0.813	0.894	0.684	0.625	12	36	0.194
chaksu_expert_2	386	0.837	0.892	0.826	0.648	0.589	7	56	0.254
chaksu_expert_5	382	0.893	0.456	0.987	0.602	0.588	37	4	0.209
<i>REFUGE readers</i>									
refuge_expert_1	452	0.942	0.793	0.964	0.780	0.747	12	14	0.100
refuge_expert_2	446	0.926	0.787	0.942	0.692	0.657	10	23	0.122
refuge_expert_4	471	0.828	0.797	0.833	0.557	0.497	13	68	0.272
refuge_expert_7	431	0.889	0.580	0.929	0.547	0.485	21	27	0.191
refuge_expert_5	484	0.833	0.873	0.828	0.542	0.512	7	74	0.258
refuge_expert_6	447	0.810	0.875	0.801	0.536	0.496	7	78	0.293
refuge_expert_3	443	0.745	0.745	0.745	0.383	0.327	12	101	0.396

Per-expert operating-point heterogeneity. Table 7 shows that expert variation is not merely a difference in aggregate F_1 ; it reflects distinct diagnostic styles, tolerance to false positives versus false negatives, and implicit decision thresholds. This observation is consistent with prior glaucoma-reader studies. Matched-subset F_1 ranges from 0.38 to 0.78 among REFUGE readers and from 0.60 to 0.86 among CHAKSU readers, indicating substantial reader-quality heterogeneity. More importantly, the sensitivity–specificity profiles reveal different clinical operating points. For example, chaksu_expert_5 is highly specific (0.987) but has low sensitivity (0.456), suggesting a conservative threshold for calling glaucoma. In contrast, chaksu_expert_2 has much higher sensitivity (0.892) but lower specificity (0.826) and many more false positives, corresponding to a more referral-tolerant style. Similar patterns appear in REFUGE: experts 5 and 6 preserve high sensitivity but incur many false positives, whereas expert 7 is more specificity-preserving but misses more glaucomatous cases. Thus, the available readers differ not only in accuracy but also in the types of diagnostic errors they tolerate.

This heterogeneity motivates the design of MPD²-Router. A single pooled “human expert,” majority vote, or unstructured defer action cannot represent these reader-specific operating points. The best-oracle row in Table 7 is not a deployable method, but it is informative: reader errors are not perfectly aligned, so the most useful human reviewer is case-dependent. MPD²-Router directly targets this setting by separating whether to defer, through d_i , from whom to defer to, through the conditional masked allocation q_i . The router can therefore learn when human review has positive marginal

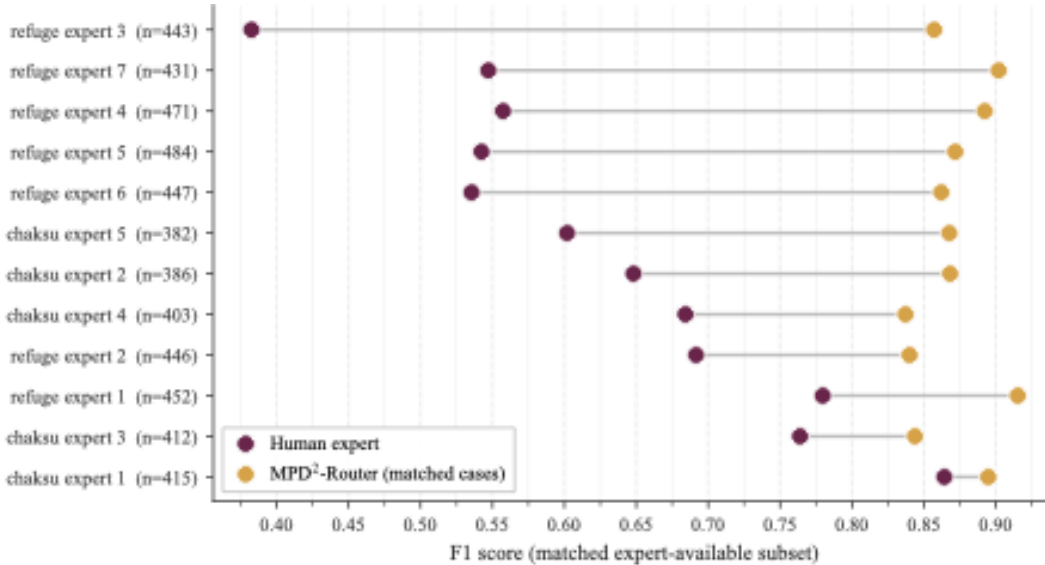


Figure 6: Matched-subset F_1 comparison between individual human experts and MPD²-Router. Each row evaluates one expert and MPD²-Router on the same cases where that expert is available; n denotes the matched availability size, and grey lines show the F_1 gap.

value and which available expert is most appropriate for the case, rather than treating all experts as exchangeable.

Matched comparison with MPD²-Router. Figure 6 compares each individual reader with MPD²-Router on exactly the same matched cases. MPD²-Router improves matched-subset F_1 in all 12/12 expert pairings, with gains as large as +0.48 over the weakest reader and a positive gain even over the strongest reader. The smaller gap near the best CHAKSU reader reflects a natural ceiling effect, but the dominance remains strict. This shows that MPD²-Router is not simply compensating for weak annotators; it adds complementary, risk-aware routing signal even when the available human prior is strong.

Spatial evidence for selective deferral. Figure 7 resolves the same comparison over a two-dimensional embedding of the test distribution. The mean available-human accuracy appears high across much of the manifold, but this aggregate view masks the per-expert heterogeneity quantified in Table 7. In contrast, the frozen AI classifier exhibits a localized failure region where accuracy collapses. MPD²-Router largely recovers this region, leaving residual errors sparse rather than spatially clustered. Its deferral mass is concentrated on the AI failure region and suppressed where the frozen classifier is already reliable. Thus, MPD²-Router does not spend expert capacity uniformly or merely to satisfy a budget; it makes selective, Pareto-favorable human–AI routing decisions by allocating expert review where the expected marginal clinical value is highest.

Together, the matched-subset, operating-point, and spatial analyses support the central claim of MPD²-Router: glaucoma deferral is not a binary choice between AI and a homogeneous human fallback. It is an instance-wise, mask-aware allocation problem under heterogeneous reader behavior, asymmetric diagnostic harm, and localized model failure. MPD²-Router improves over every individual expert on that expert’s own available cases precisely because it learns this structured human–AI complementarity.

H Dataset details.

Dataset access, licenses, and terms of use. We use only previously released ophthalmic datasets and credit the original creators in all cases. Raw fundus images and raw annotations are not redistributed with this submission. Instead, we provide preprocessing scripts, configuration files, split identifiers, and instructions for obtaining each dataset from its original source, so that users can

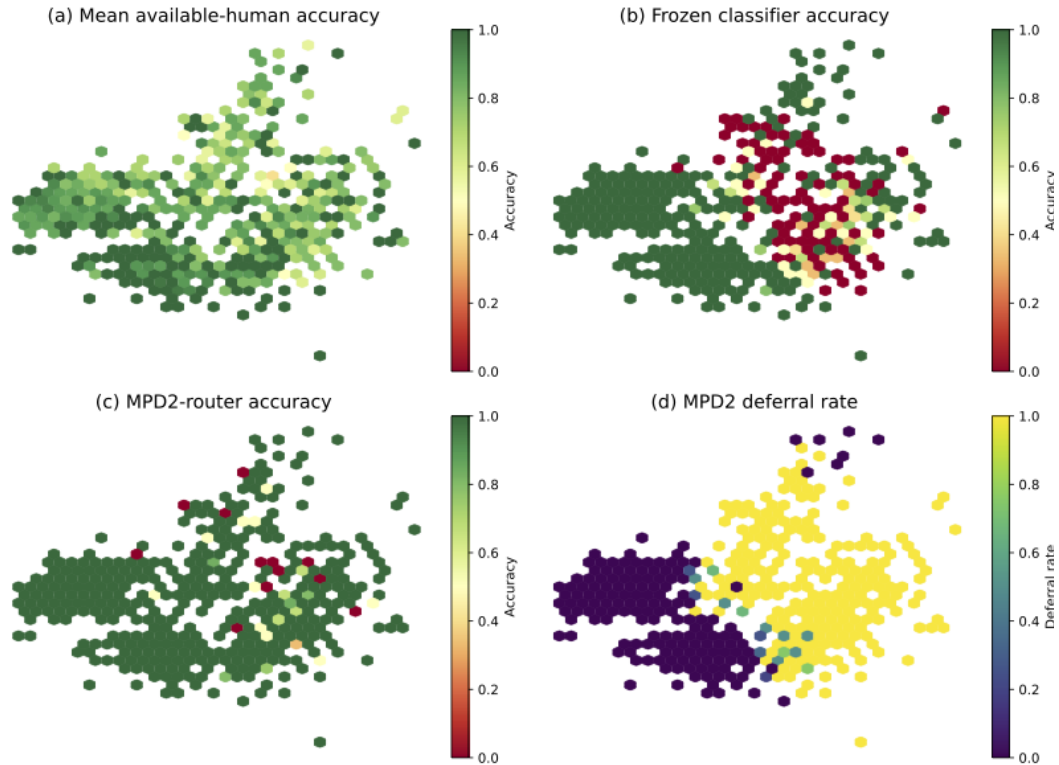


Figure 7: Spatial performance map over the test distribution. MPD²-Router concentrates deferral on localized AI failure regions while preserving AI decisions in regions where the frozen classifier remains reliable.

reproduce the experiments after agreeing to the corresponding dataset terms. All datasets were used only for non-commercial academic research. No web-scraped medical images are used.

Preprocessing and reproducible splits. For each dataset, we preserve the original image identifiers and construct a single fixed split used throughout all experiments. REFUGE follows the official challenge split when training and validating the frozen AI model. CHAKSU follows the released train/test organization where applicable. For ORIGA, which does not provide dense multi-expert routing labels, we use a fixed stratified split with the same random seed across all methods.

Use of existing code and model assets. All third-party software libraries and pretrained backbones used for feature extraction or initialization are cited in the main paper or implementation appendix, together with their versions and licenses where available. The proposed MPD²-Router training code, prior construction, mask-aware routing logic, and evaluation scripts are our own implementation. No external clinical decision model is redistributed as part of this submission unless explicitly permitted by its license.

Table 8: Public ophthalmic datasets and asset-use information. We do not redistribute raw medical images or annotations; users must obtain each dataset from the original source and follow the corresponding license or access terms.

Dataset	Source and credit	Annotations used in this work	Access, license, and redistribution
REFUGE	REFUGE Retinal Fundus Glaucoma Challenge [Orlando et al., 2020]; official challenge page: https://refuge.grand-challenge.org/ ; Figshare DOI: https://doi.org/10.6084/m9.figshare.26049574 .	Color fundus images, clinical glaucoma labels, and optic-disc/optic-cup annotations. REFUGE provides 1200 images with official train/validation/test subsets; in our work it is also used to train the frozen AI backbone and to derive structural features for routing.	Released on Figshare under Creative Commons Attribution 4.0 International (CC BY 4.0). Available from the original challenge/data-hosting platform under its access terms. We do not redistribute raw REFUGE images or annotations.
CHAKSU	Chákṣu IMAGE dataset [Kumar et al., 2023]; Figshare DOI: https://doi.org/10.6084/m9.figshare.20123135 .	1345 Indian-ethnicity fundus images acquired using three fundus-camera types, with optic-disc/optic-cup contours and binary glaucoma decisions from five expert ophthalmologists. We use the per-expert decisions and annotations for multi-expert routing supervision.	Released on Figshare under Creative Commons Attribution 4.0 International (CC BY 4.0). We cite the dataset and do not redistribute raw images in our supplementary material.
ORIGA-light	ORIGA-light dataset [Zhang et al., 2010]. Figshare DOI: https://doi.org/10.6084/m9.figshare.20123135	650 Singaporean fundus images with image-level glaucoma labels and optic-disc/optic-cup annotations. ORIGA does not provide the dense multi-expert decision structure required for direct expert-allocation supervision, so we use it as an expert-sparse cross-cohort evaluation setting.	Released on Figshare under Creative Commons Attribution 4.0 International (CC BY 4.0) and available through the original data-owner access/request procedure or the specific public repository used by the researcher. We do not claim ownership or redistribute raw ORIGA images.